Journal of Nanobiotechnology

RESEARCH

Open Access

Multifunctional hydrogel with mild photothermal properties enhances diabetic wound repair by targeting MRSA energy metabolism

Qian Gao[1], Fangfang Hu[1], Zihan Chai[1], Caiyun Zheng[1], Wenhui Zhang[1], Ke Pu[1], Ziyi Yang[1], Yanni Zhang[1], Seeram Ramrkrishna[2], Xianglong Wu[1*] and Tingli Lu[1*]

Abstract

Background Diabetic wound infections, exacerbated by multidrug-resistant pathogens like MRSA, remain a critical challenge due to biofilm persistence and dysregulated oxidative-inflammatory-metabolic crosstalk.

Results In this work, we engineered COG-Z@P200 hydrogel, a chitosan-based hydrogel integrating polydopamine-coated ZIF-8 nanoparticles, to synergize mild photothermal therapy (40–45 °C) with metabolic-immune reprogramming. Upon NIR irradiation, COG-Z@P200 disrupted MRSA through Zn^{2+}-mediated membrane destabilization and localized hyperthermia, achieving >99.5% eradication via combined physical puncture and metabolic interference. Multi-omics analyses revealed suppression of glycolysis *(eno, gap* downregulation), TCA cycle arrested (*sucC, sdhA, icd* inhibition), and disruption of arginine biosynthesis (*arcA*, *arcC*, *arcD* downregulation), impairing biofilm formation and pathogenicity. Concurrent silencing of quorum sensing and virulence genes (*agr, sec, lac, opp, sdrD*) further destabilized MRSA, while upregulation of stress-response genes (*yidD, nfsA, kdpA*) indicated bacterial metabolic paralysis. In diabetic murine models, the hydrogel attenuated oxidative stress (DHE-confirmed ROS reduction), polarized macrophages to pro-healing M2 phenotypes (Arg-1^{+}/TNF-α↓), and enhanced angiogenesis (VEGF/CD31↑) alongside aligned collagen deposition. This multifunctional action accelerated wound closure by 48% versus controls, outperforming clinical standards. By converging nanomaterial-enabled bactericidal strategies with host microenvironment recalibration, COG-Z@P200 hydrogel redefined diabetic wound management, offering an antibiotic-free solution against multidrug-resistant infections.

Conclusion Our work established a biomaterial paradigm that concurrently targets pathogen vulnerabilities and restores tissue homeostasis, addressing the multidimensional complexity of chronic wounds.

Keywords Multifunctional hydrogel dressing, ZIF-8 nanoparticles, Photothermal therapy, Metabolic interference, Diabetic wound microenvironment

*Correspondence:
Xianglong Wu
wuxianglong@nwpu.edu.cn
Tingli Lu
lutinglixinxin@nwpu.edu.cn
Full list of author information is available at the end of the article

Introduction

Diabetic wound infections (such as diabetic foot ulcers) have become a major burden on global public health due to their high risk of complications and prolonged non-healing characteristics [1, 2]. Hyperglycemia, excessive accumulation of reactive oxygen species (ROS) and infection with multidrug-resistant bacteria (such as MRSA) in the chronic wound microenvironment jointly lead to inflammatory disorders [3–6], blocked angiogenesis and failure of extracellular matrix (ECM) remodeling, ultimately forming a vicious cycle [5–10]. Traditional treatment strategies (such as systemic administration of antibiotics and local debridement) are often limited in efficacy due to the inability to simultaneously regulate the microenvironment, especially the synergistic deterioration of drug-resistant bacterial infection and high-sugar microenvironment [3, 11–13]. Therefore, the development of new multifunctional therapeutic platforms to simultaneously address infection control, metabolic regulation and tissue regeneration has become a core direction of current research [7, 14–16].

Photothermal agents (PTAs) such as polydopamine (PDA), a natural analog of melanin, have shown great potential as effective PTAs due to their ease of synthesis, excellent photostability, biodegradability, and biocompatibility [17–19]. PDA can convert light energy into heat, leading to bacterial cell membrane damage, DNA damage, protein denaturation, and subsequent bacterial death. However, conventional PTT often requires temperatures above 60 °C, which can damage healthy tissues and limit its therapeutic potential in vivo [20]. Recent studies suggest that maintaining temperatures below 50 °C can minimize damage to normal tissues while still achieving effective bacterial eradication [21, 22].

In addition to PTT, Zeolitic Imidazolate Framework-8 (ZIF-8) has emerged as a promising material for wound healing applications. ZIF-8 is a metal–organic framework (MOF) known for its high specific surface area, porosity, and excellent biocompatibility, making it an ideal candidate for drug delivery and antibacterial applications [23]. ZIF-8 exerts its antibacterial effect by disrupting bacterial cell membranes and generating reactive oxygen species (ROS), which inhibit bacterial growth and reduce the risk of infection [24, 25]. Moreover, ZIF-8 can be utilized as a carrier for the controlled release of growth factors, anti-inflammatory agents, and antimicrobial drugs, thereby promoting wound healing and tissue regeneration [26]. Despite the potential of ZIF-8, its application in wound healing has been limited by several challenges, including its stability and the need for more efficient antibacterial strategies. To address these limitations, multicomponent synergistic therapies have emerged as a promising solution. By combining various therapeutic components, such as metal nanoparticles, PDA, and hydrogels, it is possible to enhance the antibacterial effect, reduce the risk of bacterial resistance, and accelerate wound healing [27–29]. For example, metal nanoparticles, such as those incorporated in hydrogels, can enhance the PTT effect by preventing nanoparticle aggregation, improving the porosity structure [28, 29], and providing mild antibacterial properties at low temperatures.

This study presents a multifunctional hydrogel dressing (COG-Z@P200 + NIR5) engineered to accelerate diabetic wound healing through synergistic metabolic intervention and dynamic microenvironment regulation. The hydrogel integrates dopamine-modified ZIF-8 nanoparticles with a double-crosslinked framework composed of carboxymethyl chitosan (CMCS), gelatin, and oxidized sodium alginate (OSA). CMCS disrupts bacterial membranes via Zn^{2+} release and synergizes with near-infrared (NIR)-triggered mild photothermal therapy (40–45 °C), achieving dual bactericidal action through physical puncture and metabolic interference. Gelatin enhances biocompatibility and mechanical adhesion, while OSA reinforces structural stability. The hydrogel's therapeutic efficacy arises from three interconnected mechanisms: NIR-activated hyperthermia disrupts MRSA energy metabolism by suppressing glycolysis (*eno, gap*) and quorum sensing (*agr*), immunomodulatory polarization of macrophages toward M2 phenotypes (Arg-1^+/TNF-α↓) promotes angiogenesis (VEGF/CD31↑) and collagen alignment, and pH-responsive ROS scavenging with ECM remodeling dynamically adapts to microenvironmental fluctuations. Validated in diabetic murine models, COG-Z@P200 + NIR5 reduced healing time by 48% and eradicated >99.5% MRSA, outperforming clinical benchmarks. This work establishes an antibiotic-free paradigm for chronic wound management, bridging nanomaterial-enabled bactericidal strategies with host-directed metabolic-immune crosstalk, and offers a scalable solution for multidrug-resistant infections in hyperglycemic niches.

Materials and methods

Materials and instruments

Zinc nitrate hexahydrate ($Zn(NO_3)_2{\cdot}6H_2O$, 99.9%), 2-methylimidazole (2-MIm), carboxymethyl chitosan (CMCS, Shanghai yuanye Bio-TechnologyCo., Ltd. carboxylation degree ≥80%, Mw = 650 kDa), Sodium alginate (SA, Aladdin™, assay ≥98%, viscosity 350–550 mPas, Mw = 100–150 kDa, M:G ratio = 1:1), pig skin-derived gelatin (Gel, type A), dopamine (DA, purity ≥99%), streptozotocin (STZ, Beijing Solebao), sodium hydroxide (NaOH), ethanol (C_2H_5OH), β-galactosidase kit (β-galactosidase, Beyotime, Haimen, China), 2′,7′-dichlorodihydrofluorescein diacetate detection kit (DCFH-DA, Beyotime, Haimen, China), enhanced ATP

detection kit (Beyotime, Haimen, China). All chemicals and reagents were employed as received unless stated otherwise. X-ray diffraction (XRD, D8 Advance, Bruker, Germany). Transmission electron microscope (TEM, JEOL JEM-F200, Japan). Scanning Electron Microscope (SEM, ZEISS Sigma 300, Germany). X-ray photoelectron spectroscopy (XPS, ESCALAB 250Xi, Thermo Scientific, USA).

Synthesis of ZIF-8@PDA nanoparticles

Based on previous studies, we synthesized ZIF-8 nanoparticles with a particle size of around 533 nm through an enhanced solvothermal technique [30]. Subsequently, 20 mg of ZIF-8 particles were suspended in 100 ml of 10 mM Tris–HCl solution at pH 8.5. Subsequently, 0.2 g of dopamine hydrochloride was included and agitated for 10 min until fully dissolved. The pH was subsequently adjusted to 8.5, and the mixture was agitated for 6 h at ambient temperature in darkness. Subsequently, the mixture underwent centrifugation and was rinsed three times with deionized water to eliminate any unpolymerized dopamine. The black ZIF-8@PDA particles were produced ultimately. The comprehensive preparation protocols are outlined in the Supporting Information.

Synthesis and characterization of COG-Z@P hydrogel

Various concentrations of ZIF-8@PDA nanoparticles (50, 100, 150 and 200 μg//mL) were dissolved in CMCS and thoroughly mixed. Subsequently, 10% gel (w/v) and the pre-prepared OSA solution (15%, w/v) were included. The solution was stirred vigorously under vortex conditions until gelation occurred, OSA is chemically double-cross-linked with Gel and CMCS via a dynamic Schiff base reaction to generate COG-Z@P hydrogel (COG hydrogel does not contain ZIF-8@PDA NPs).

Rheological assessments were performed with a rheometer (MCR 302) to evaluate the mechanical characteristics of hydrogels. The hydrogel was made in circles with a diameter of 1.5 cm and a thickness of 1–2 mm, and it was examined at 37 °C using a time-oscillating scan at 1 Hz and 1% strain. The variations in storage modulus (G') and loss modulus (G'') were quantified, respectively. The self-repairing capabilities of hydrogels were evaluated by the oscillatory strain scanning technique. The test cycle comprised a modest strain ($\gamma = 1\%$) at a constant frequency of 1 rad/s for 100 s, thereafter transitioning to a large strain ($\gamma = 400\%$) for an additional 100 s. This cycle was reiterated 2.5 times. The macroscopic self-healing characteristics of hydrogels were assessed utilizing two hydrogel discs: a brownish-black disc (Z@P-COG200) and a light yellow disc (COG). The hydrogels were bisected, and the semicircular segments of varying colors were aligned along the incision. The hydrogels were incubated at 37 °C for 30 min, following which they were removed. The technique was documented through video and photography to capture the self-healing characteristics of the hydrogel.

In vitro photothermal and antibacterial properties

1 mL of ZIF-8@PDA nanoparticles at varying concentrations (50, 100, 150 and 200 μg/mL) was distributed in either ultrapure water or COG hydrogel. The experiment was performed in a 24-well plate. Thereafter, the samples were exposed to a near-infrared laser (808 nm, 1 W/cm^2) for 10 min, utilizing ultrapure water or COG hydrogel as controls. Temperature variations were documented via an infrared thermal imaging camera. The photothermal stability of the nanoparticles was assessed by comparing the temperature profiles prior to and following near-infrared irradiation, in addition to after four heating and cooling cycles. Gram-negative *E. coli* and drug-resistant MRSA bacteria were tested in vitro to assess the material's antibacterial activity. The MARS infected wound model was employed to evaluate the in vivo antibacterial efficacy of the hydrogel. The comprehensive processes are presented in the Supporting Information.

Transcriptomic analysis

Total RNA isolation, cDNA library construction, and sequencing

MRSA cultures were exposed to Z@P-COG200 + NIR for 5 min, with PBS-treated bacterial suspensions serving as negative controls. Bacterial pellets were harvested via centrifugation at 6,000×*g* (4 °C, 5 min) and subjected to three sequential PBS washes. Three biological replicates per group (Control: CTRL1, CTRL2, CTRL3; Experimental: Sample1, Sample2, Sample3) were processed under standardized conditions. Total RNA was extracted using TRIzol® reagent, with RNA integrity confirmed by Bioanalyzer (RIN > 8.0). Strand-specific cDNA libraries were constructed following Illumina® TruSeq™ Stranded Total RNA Library Prep Kit protocols (Majorbio Bio-pharm Technology, Shanghai, China), including ribosomal RNA depletion via Ribo-Zero™ Gold rRNA Removal Kit. Libraries were quantified by Qubit® 4.0 Fluorometer and size-validated by Agilent 2100 Bioanalyzer. Paired-end sequencing (2 × 150 bp) was performed on an Illumina NovaSeq 6000 platform (Majorbio Bio-pharm Technology) with a minimum depth of 20 million reads per sample.

Differentially expressed genes (DEGs) screening and bioinformatics analysis

Following normalization and variance stabilization of raw count data using DESeq2 (v1.24.0), differentially expressed genes (DEGs) were identified through a

rigorous statistical framework incorporating Benjamini–Hochberg multiple testing correction. Genes meeting the threshold of absolute log2 fold change (|log2 FC|) ≥1 and adjusted p-value (padj) <0.05 were classified as significant DEGs. Functional annotation was performed through hierarchical orthologous group classification via the Clusters of Orthologous Genes (COG) database (v5.0) and pathway enrichment analysis using the Kyoto Encyclopedia of Genes and Genomes (KEGG) database (Release 107.1). Enrichment significance was assessed via hypergeometric testing with false discovery rate (FDR) correction (q-value <0.05), as implemented in the clusterProfiler R package (v4.6.2).

Metabolomic analysis

Metabolite extraction and LC–MS-based untargeted metabolomics analysis

Metabolomic sample preparation followed the protocol in Transcriptomic analysis, with six biological replicates per group (Control: CTRL1, CTRL2, CTRL3, CTRL4, CTRL5, CTRL6; Experimental: Sample1, Sample2, Sample3, Sample4, Sample5, Sample6). Metabolites were extracted using 400 µL of 80% methanol containing 0.02 mg/mL L-2-chlorophenylalanine (internal standard). Tissues were homogenized in a cryogenic grinder (−10 °C, 50 Hz, 6 min), sonicated (40 kHz, 30 min) at 5 °C, incubated at −20 °C for 30 min, and centrifuged (13,000×*g*, 15 min, 4 °C). The supernatant was analyzed via LC–MS (Thermo Scientific Vanquish Horizon UHPLC-Q-Exactive system) by Majorbio Bio-pharm Technology (Shanghai, China).

Differentially expressed metabolites (DEMs) screening and bioinformatics analysis

Raw metabolomics data were analyzed using Progenesis QI (Waters Corporation, USA). Metabolite identification was conducted via HMDB and MetLin databases, followed by pathway annotation using KEGG (http://www.genome.jp/kegg/). Differential metabolites (DEMs) were screened with the *ropls* R package (v1.6.2), applying thresholds of $p < 0.05$ and variable importance in projection (VIP) >1.

Biocompatibility of hydrogels

Cytocompatibility study

The substance underwent sterilization, and the extract was procured. Cells were inoculated at a density of 2.0×10^4 cells/cm^2 and incubated under regulated conditions. To evaluate the proliferation of L929 cells co-cultured with different hydrogels after 1, 2 and 3 days, 10% MTT in serum-free medium was introduced to each well, followed by a 4-h incubation. Subsequently, DMSO was added, and the plate was agitated for 10 min. The absorbance at 490 nm was then quantified using a multifunctional microplate reader.All trials were conducted in quintuplicate, and the mean value was utilized as the final result. Cell cytotoxicity was evaluated using a Calcein-AM/PI dual staining kit. A Leica MD IL inverted fluorescent microscope was used to observe live cells at 495 nm/515 nm (excitation/emission) and dead cells at 495 nm/635 nm.

Blood compatibility study

A hemolytic activity assay was conducted to evaluate the blood compatibility of the hydrogel. C57/BL6 diabetic mice were anesthetized, and blood was obtained from the abdomen vein using a blood collection tube. A blood dilution was created by combining 4 mL of mouse blood with 5 mL of PBS. Subsequently, 500 µL of various hydrogels and 500 µL of the blood dilution were combined in a 1.5 mL centrifuge tube and incubated at 100 rpm in a stirrer at 37 °C for 1 h. Following incubation, the tube was centrifuged at 1,000 rpm for 10 min, and 100 µL of the supernatant was aliquoted into a 96-well plate. The absorbance of the solution at 540 nm was assessed utilizing a multifunctional enzyme marker. A positive control comprised 500 µL of water, whereas a negative control comprised 500 µL of PBS buffer. The hemolysis rate was ultimately determined using Eq. (1):

$$\text{Hemolysis ratio} = (A_e - A_p/A_w - A_p) \times 100\% \quad (1)$$

Ae—represents absorbance of the experimental group; Ap—denotes absorbance of the negative control group; Aw—signifies absorbance of the positive control group.

Construction of whole skin wound model in diabetic mice infected with MRSA

All animal experiments were conducted in strict accordance with the National Regulation of China for the Care and Use of Laboratory Animals, as well as the National Research Council Guidelines for the Care and Use of Laboratory Animals. The study was approved by the Ethics Committee for Medical and Experimental Animals at Northwestern Polytechnical University (Approval No. 202202091). C57/BL6 male mice (SPF, male, 6–8 weeks old) were acquired from the Animal Experiment Center at Xi'an Jiaotong University. The mice were given D12492 high-sugar, high-fat standard food and plenty water for one week. The fasting blood glucose levels of mice were measured after a 12-h fast. Thereafter, the mice were weighed and administered an intraperitoneal injection of a prepared streptozotocin (STZ, Solarbio) solution at a dosage of 55 mg/kg for five consecutive days. One week later, the mice underwent fasting blood glucose testing via blood collection

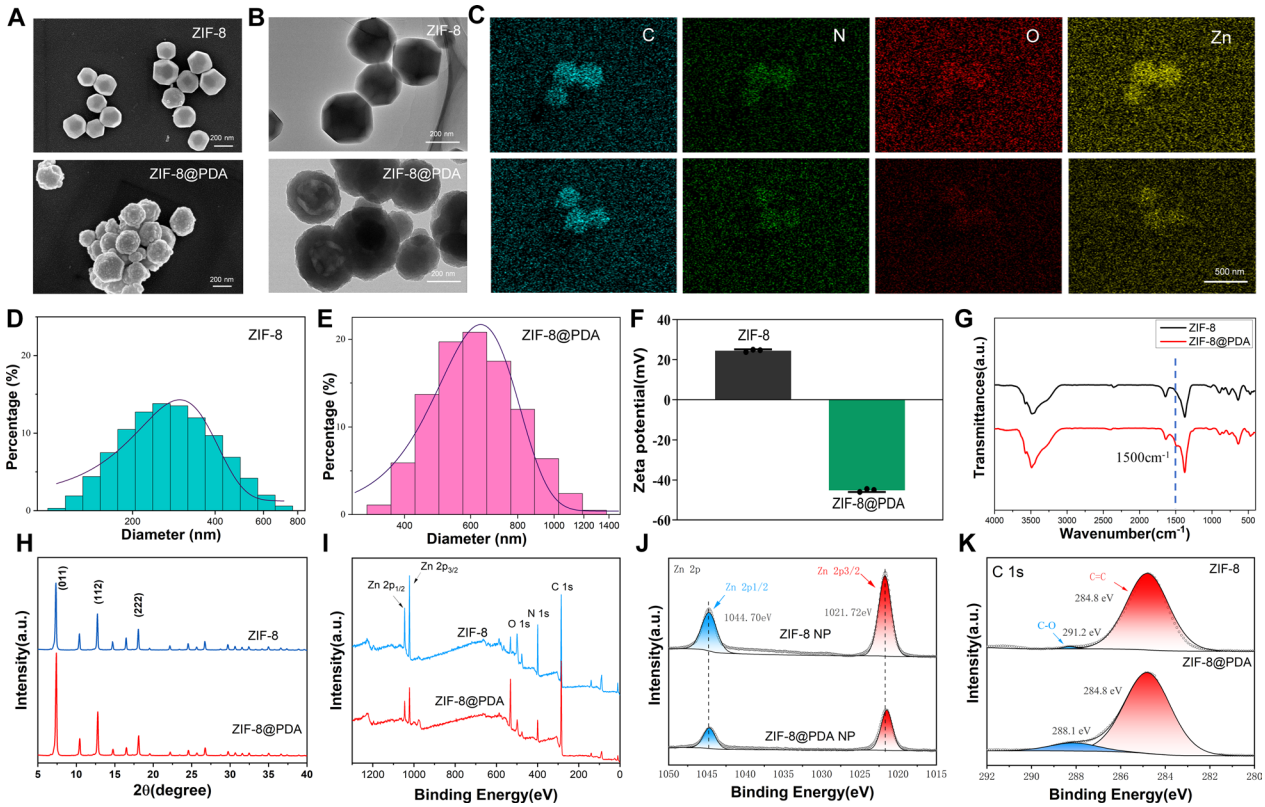

Fig. 1 Characterization of ZIF-8 NPs and ZIF-8@PDA NPs. **A**–**B** SEM and TEM. Scale = 200 nm. **C** Mapping of element. Scale = 50 nm. **D**–**E** Particle size distribution. **F** Zeta potentials. **G** FT-IR spectrum. **H**–**K** XRD and XPS analysis

from the tail vein. Blood glucose levels surpassing 16.7 mmol/L, along with noted weight loss and polyuria, confirmed the effective establishment of the diabetic mouse model.

A 0.3% sodium pentobarbital solution (0.1–0.2 mL/10 g) was administered to anesthetize the mice. A 6 mm diameter punch was employed to generate a circular wound on the backs of mice, then followed by the application of 20 μL of Staphylococcus aureus (1×10^8 CFU/mL) drops onto the wound surface to construct a full-thickness skin injury infection model. Mice were randomly allocated into five groups: Control group, COG group, COG + NIR5 group, COG-Z@P200 group, and COG-Z@P200 + NIR5 group.

To evaluate wound tissue regeneration (epidermal thickness, new granulation tissue, and collagen deposition), mice were euthanized on days 3, 7 and 14, and skin tissues were harvested. The collected tissues were fully submerged in 4% paraformaldehyde (G1101, Servicebio) for fixation, then embedded in paraffin, sectioned, and stained using hematoxylin–eosin (H&E, GP1031, Servicebio) and Masson's trichrome staining kit (G1006, Servicebio). Images were obtained using a tissue biopsy scanner (Science, WINMEDIC) and analyzed with ImageJ software.

Statistical analysis

In this experiment, each group contained a minimum of three independent replicates. The data results were presented as mean ± standard deviation (SD). The experimental data were subjected to statistical analysis by One-way ANOVA to evaluate significant differences among groups. A $*p < 0.05$ denotes statistical significance, $**p < 0.01$ signifies a high level of statistical significance, $***p < 0.001$ represents a very high level of statistical significance, and $****p < 0.0001$ shows an extremely high level of statistical significance.

Results and discussion

Synthesis and characterization of ZIF-8 NPs and ZIF-8@PDA NPs

ZIF-8 nanoparticles were produced according to established protocols reported in the literature [31, 32]. Subsequently, DA was incorporated, resulting in the formation of ZIF-8@PDA nanoparticles (Fig. 1A). A SEM image demonstrated that ZIF-8 NPs exhibited a normal dodecahedron shape (Fig. 1A-a1), but ZIF-8@

PDA NPs, coated with polydopamine, presented an irregular spherical form (Fig. 1A-a2). Based on TEM morphology, ZIF-8 (Fig. 1B-b1) exhibited a uniform coloration, but ZIF-8@PDA NPs (Fig. 1B-b2) displayed a lighter hue on the surface compared to the interior. The transformation of nanoparticles from white to black, before and after polydopamine coating, was observable to the naked eye. The EDS spectra of ZIF-8@PDA NPs (Fig. 1C) indicated an elevation in carbon and nitrogen components, potentially attributable to the PDA coating. 1 mg/mL ZIF-8@PDA nanoparticles in ddH_2O were analyzed for Zeta potential and hydrodynamic particle size using a Nano-ZS dynamic light scattering instrument (Fig. 1D, E). The zeta potential of ZIF-8@PDA NPs (−45 mV) was significantly lower than that of ZIF-8 NPs (24.7 mV), indicating enhanced colloidal stability and improved dispersion of ZIF-8@PDA NPs. The average particle size of ZIF-8 NPs and ZIF-8@PDA NPs was found to be reasonably consistent in an aqueous environment, with ZIF-8 exhibiting a positive charge and ZIF-8@PDA NPs displaying a negative charge attributed to the hydroxyl groups of DA (Fig. 1F).

In comparison to ZIF-8 NPs, the FTIR spectra of ZIF-8@PDA NPs exhibited a peak at 1500 cm^{-1}, indicative of the stretching vibration of the carbon–carbon double bond (C=C group), primarily derived from the benzene ring structure of dopamine (Fig. 1G). The characteristic XRD peaks of ZIF-8 are seen in the XRD patterns of NPs (Fig. 1H) at 2θ angles of 7.20°, 12.60°, and 17.90°. These angles correspond to the (110), (211), and (222) crystallographic planes [33]. The crystal morphology of ZIF-8 was confirmed, and the peak position exhibited minimal alteration before and after dopamine coating. The chemical composition and electrical structure of ZIF-8 nanoparticles exhibited significant alterations for dopamine encapsulation, as demonstrated by XPS (Fig. 1I). ZIF-8@PDA NPs comprised zinc (Zn), oxygen (O), carbon (C), and nitrogen (N). The zinc ions exhibited two peaks (Fig. 1J) at 1022 and 1045 eV, corresponding to the $2p_{3/2}$ and $2p_{1/2}$ orbitals, respectively. Simultaneously, the C1 s peak bifurcated into two components at 284.8 and 291.2 eV, associated with the C–C and C–N bonds (Fig. 1K). The characteristic N1 s and Zn 2p peaks remained following dopamine encapsulation, indicating that ZIF-8@PDA nanoparticles have a stable framework structure. The characteristic N1 s and Zn 2p peaks remained following dopamine encapsulation, indicating that ZIF-8@PDA nanoparticles have a stable framework structure. Previous findings indicated that the N1 s XPS spectrum exhibited two peaks at 400.98 and 399.38 eV (Figure S1 A), corresponding to C=N and C–N in 2-methylimidazole. Additionally, a novel signal associated with C=O at 531.73 eV (Figure S1B) suggests the potential presence of polydopamine on the surface of ZIF-8.

Preparation and structural characterization of COG-Z@P hydrogels

An environmentally sustainable one-pot method was employed to incorporate varying concentrations of Z@P nanoparticles into COG, resulting in hydrogels designated as COG-Z@P50, COG-Z@P100, COG-Z@P150 and COG-Z@P200. The COG hydrogel was synthesized by doubly cross-linking the aldehyde group of oxidized sodium alginate (OSA) with the amino groups of CMCS and gelatin via a Schiff base reaction (Fig. 2A). OSA was synthesized through the oxidation of sodium alginate (SA), as described in previous studies [34]. The FTIR spectrum of OSA exhibited a unique absorption band at 1720 cm^{-1}, corresponding to the stretching vibration of the (−CHO) C=O bond in the SA aldehyde group (Figure S2 A). The oxidation degree of OSA was found to be 27.28% (Figure S2B), determined via the hydroxylamine hydrochloride reaction, which facilitated the subsequent Schiff base reaction.

ZIF-8@PDA nanoparticles were incorporated into CMC to produce a fluid black suspension, as shown in Fig. 2B. This suspension was then combined with the OSA solution and rapidly mixed. The COG-Z@P200 hydrogel was synthesized in less than 10 s. For comparison, the COG hydrogel was synthesized without the addition of ZIF-8@PDA nanoparticles. Both hydrogels exhibited a homogeneous, porous, and interconnected network structure, with ZIF-8@PDA nanoparticles uniformly distributed (Fig. 2C, red arrow). The self-healing properties of the hydrogels were evaluated by bisecting a black COG-Z@P200 hydrogel disc and a transparent COG hydrogel. The two resulting semicircular hydrogel pieces were placed in contact along the cutting line to assess the reformation of the gel. As shown in Fig. 2D, within 30 min, the two halves autonomously reassembled into a complete hydrogel with distinct colors. The reformed hydrogel demonstrated excellent self-healing capabilities, maintaining structural integrity when stretched with forceps perpendicular to the incision line.

Mechanical properties and self-healing properties

Three distinct hydrogel samples were subjected to dynamic frequency scanning experiments, resulting in the storage modulus (G′) and loss modulus (G″), along with the rheological test results, as presented in Fig. 2E. All hydrogels exhibited G′ values exceeding G″ throughout the entire testing range, demonstrating robust gel strength and a stable gel state. The G′ and G″ values of the COG hydrogel increased with frequency, indicating

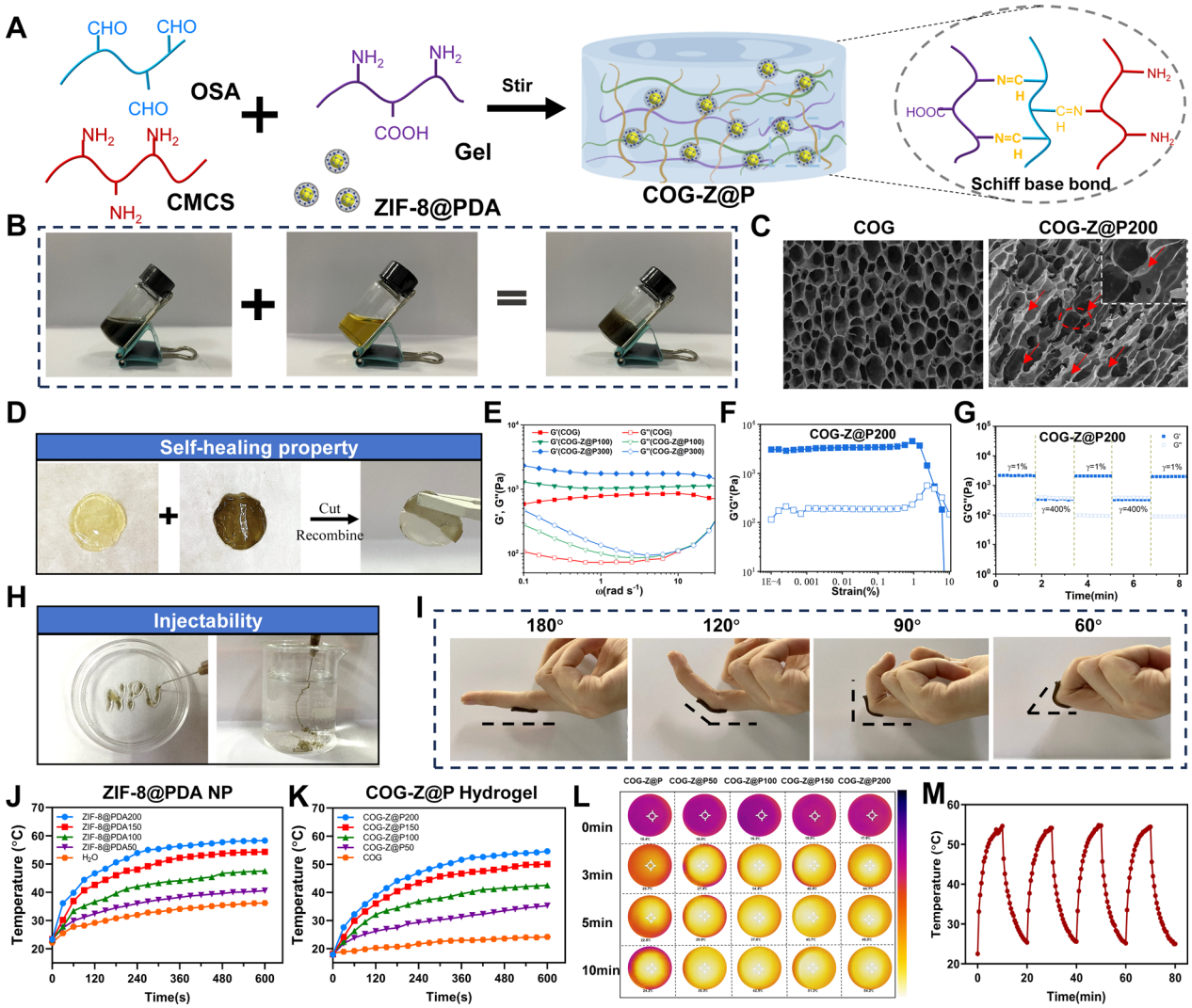

Fig. 2 Preparation and characterization of COG-Z@P200 hydrogel. **A**–**B** Schematic diagram of hydrogel synthesis; **C** SEM image; **D** Frequency scan; **E** Dynamic strain scan test; **F** Cyclic scan test under shear strains of 1 and 400% (ω = 1 rad/s); **G** Self-healing performance; **H** Demonstration of injectability of hydrogel; **I** Adhesion and tensile properties; **J**–**K** Thermal infrared image of COG-Z@P hydrogel under NIR radiation. **L** Temperature change curves of different concentrations of ZIF-8@PDA NPs and COG-Z@P hydrogels with laser irradiation time. **M** Temperature changes of COG-Z@P200 hydrogel during four cycles of on/off 1.0 W cm^{-2}, 808 nm laser irradiation

physical entanglement within the network of reversible dynamic chemical cross-linking. However, the G′ and G″ values of the hydrogel samples COG-Z@P100 and COG-Z@P200 remained largely unchanged. This resulted mainly from the stable network structure and elevated cross-linking density generated by the higher concentration of ZIF-8@PDA NPs. The COG hydrogel exhibited a storage modulus greater than its loss modulus throughout the entire testing range, suggesting that the hydrogel possesses significant gel strength and maintains a stable gel state. As illustrated in Figures S3 A-B and 2F, the storage modulus (elastic modulus) of COG, COG-Z@P100 and COG-Z@P200 hydrogels was 808.21, 1040.3 and 1748.3 Pa, respectively, at a frequency of 1 rad/s. This indicates that an increase in the content of ZIF-8@PDA nanoparticles correlates with a rise in cross-linking density and the elastic modulus of the hydrogel. The G″ values of the three hydrogels converge at a strain of 385%, indicating a transitional state between solid-like and liquid-like behavior. Complete hydrogel degradation occurred at a critical strain exceeding 385%. To evaluate the hydrogel's self-healing capability, sequential step-strain testing was performed (Figures S3 C-D and 2G). Upon an initial strain of 400%, G′ decreased significantly

from 2102.6 to 339.24 Pa, indicating the disruption of the hydrogel network. However, when the strain was reduced to 1%, G′ recovered to 2081.02 Pa, suggesting that the cross-linked network had largely reformed. After five cycles of alternating high and low strain, the G′ and G″ values of the repaired hydrogel closely resembled those in the initial cycle, confirming its robust self-healing properties.

The excellent injectability of the COG-Z@P200 hydrogel makes it particularly suitable for complex wound healing applications, including those involving irregularly shaped wounds. Using a 27-gauge needle (diameter: 0.41 mm), the hydrogel was smoothly injected to form the inscription 'NPU' without clogging (Fig. 2H). Upon injection into water, the hydrogel maintained its structural integrity, forming continuous spiral thin lines, thereby demonstrating its outstanding injectability and shape retention. This high injectability is attributed to its optimized viscosity and shear-thinning behavior, which are further enhanced by the presence of dynamic non-covalent interactions within the hydrogel network. Furthermore, the hydrogel exhibited remarkable self-healing capabilities due to the reversibility of these interactions. As shown in Fig. 2I, the hydrogel adhered firmly to human finger joints, maintaining stable attachment during flexion and extension without cracking or peeling. This strong adhesion and mechanical resilience under dynamic conditions underscore its potential for clinical applications in wound healing.

Near-infrared triggered photothermal properties and antioxidant capacity

Photothermal therapy has shown considerable potential in biomedicine, with polydopamine (PDA) capable of absorbing visible and near-infrared (NIR) light and converting it into thermal energy [35–37]. To evaluate the photothermal properties of ZIF-8@PDA nanoparticles (NPs) and COG-Z@P hydrogels, we tested their temperature responses under 808 nm NIR irradiation. As shown in Fig. 2J–K, the temperature of the system increased with rising concentrations of ZIF-8@PDA NPs after 10 min of irradiation. Notably, the COG-Z@P200 hydrogel exhibited a higher temperature rise than the ZIF-8@PDA NPs alone, with ΔT values of 38.4 and 36.1 °C, respectively (Figures S4 A-B). These findings were further confirmed by infrared thermal imaging (Fig. 2L), which showed a consistent temperature increase.

The addition of ZIF-8@PDA NPs into the COG hydrogel effectively prevented nanoparticle aggregation, which can lead to the loss of photothermal efficiency. The photothermal conversion efficiency (η) was calculated for both COG-Z@P200 and ZIF-8@PDA NPs at a concentration of 200 μg/mL under 808 nm laser irradiation, yielding values of 16.88 and 25.27%, respectively. These results indicate that the photothermal performance of the COG-Z@P200 hydrogel and ZIF-8@PDA NPs are comparable, confirming the efficacy of ZIF-8@PDA NPs as a photothermal agent in hydrogel formulations. The following Eqs. (2)–(4) were used to determine the photothermal conversion efficiency: [38, 39]

$$Q = cm\Delta T \tag{2}$$

where Q, c, m, ΔT are the total heat, specific heat (H_2O: 4200 J $kg^{-1}\cdot K^{-1}$) and gelatin: 1830 J $kg^{-1}\cdot K^{-1}$), mass, and the change of temperature, respectively. The total energy of the light could be calculated using following equation:

$$E = PSt \tag{3}$$

where P is the power density of the light, S and t are the irradiation area (S=2 cm^2) and irradiation time. The photothermal conversion efficiency of COG-Z@P200 hydrogel was calculated as follows:

$$\eta = Q/E = cm\Delta T/PSt \tag{4}$$

The maximum temperature was similarly attained after near-infrared irradiation, consistent with the first cycle, during repeated heating and cooling experiments following four "ON/OFF" cycles, indicating effective photothermal reversibility (Fig. 2M). After five minutes of exposure to 808 nm radiation, the temperature of COG-Z@P200 attained 49.5 °C. The temperature was suitable for photothermal antibacterial activity and may facilitate the rapid realization of photothermal antibacterial capabilities.

The capacity of hydrogels to scavenge free radicals (DPPH) was utilized to evaluate their antioxidant properties. The catechol group in unoxidized SA resulted in a 32.55% reduction of DPPH by COG hydrogel after 60 min of incubation, as shown in Figure S5. The free radical scavenging rates of the COG-Z@P hydrogel increased to 51.88, 51.77, 57.19, and 56.60%, respectively, upon the incorporation of ZIF-8@PDA. The catechol groups in COG-Z@P hydrogel enhance its antioxidant capacity, with an increase in ZIF-8@PDA correlating to a greater antioxidant capacity.

Antibacterial activity

This study explored the antibacterial effects of COG-Z@P200 hydrogel under 1.0 $W\cdot cm^{-2}$ NIR radiation at various conditions, including the effect of using NIR light alone. Figure 3A shows the colony distribution of *E. coli* and MRSA after 2 h of treatment under different conditions, including the control group, NIR irradiation for 5 min, and COG-Z@P200 hydrogel with or without NIR exposure. Statistical analysis revealed that NIR irradiation alone showed very weak antibacterial activity, but

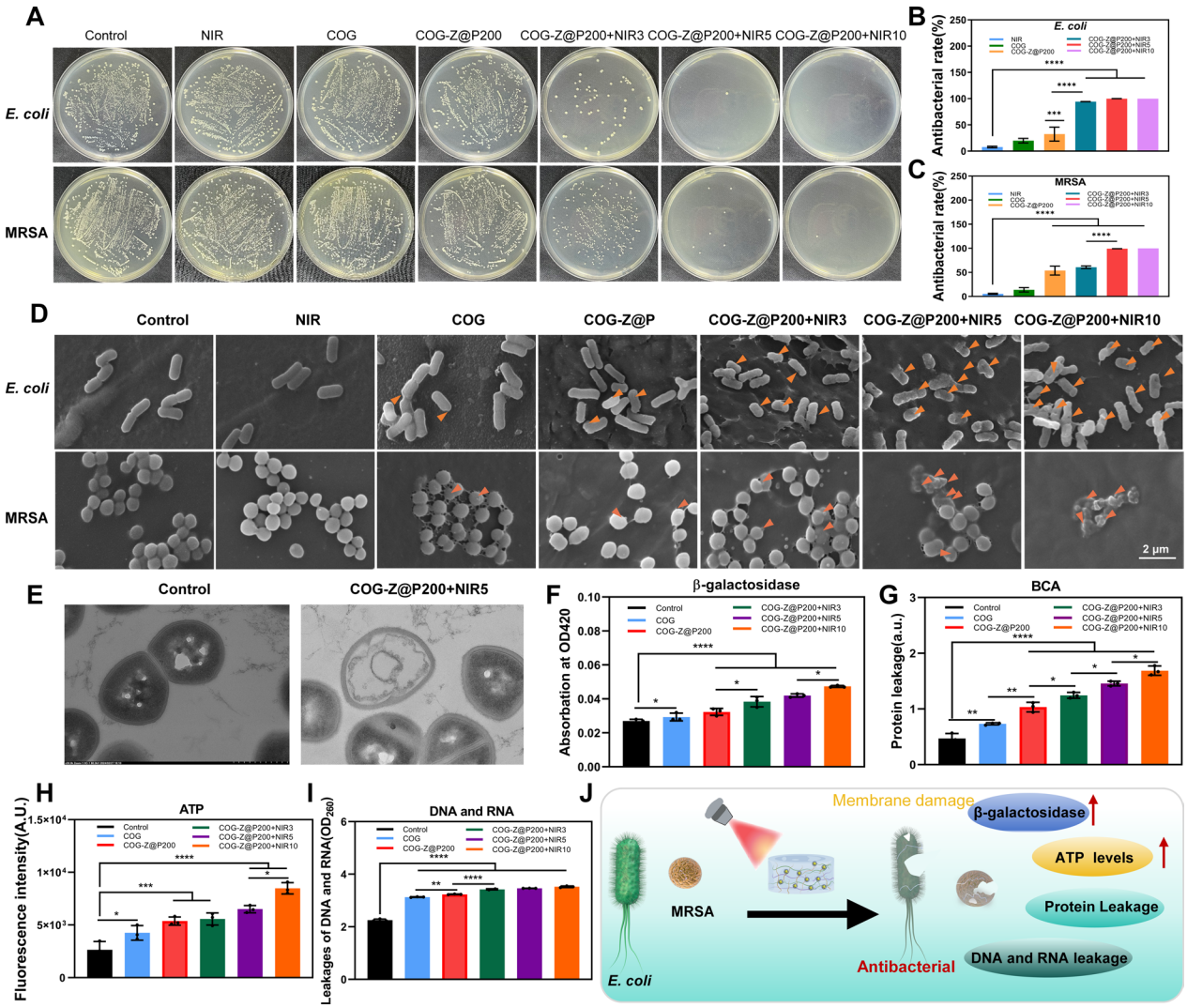

Fig. 3 Antibacterial properties of COG-Z@P200 hydrogel against *E. coil* and MARS for 2 h. **A** Colony growth of bacteria; **B**–**C** Survival rates. **D** SEM images of bacteria; **E** TEM images of bacteria. **F** β-galactosidase levels; **G** Protein leakage; **H** DNA and RNA leakage; **I** ATP levels. **J** Schematic diagram of the antibacterial mechanism and **P < 0.05, ***P < 0.001, ****P < 0.0001*

when combined with COG-Z@P200 hydrogel, the antibacterial activity was significantly enhanced (Fig. 3B–C). Moreover, the antibacterial effect continued to improve with prolonged NIR exposure. After 5 min of NIR irradiation, the hydrogel demonstrated an antibacterial efficacy exceeding 99%, with a measured temperature of approximately 49.5 °C, which remained within the safe threshold for PTT, thus preventing further harm to the body [21]. Additionally, the incorporation of ZIF-8@PDA nanoparticles into the COG hydrogel significantly enhanced its antibacterial effect against MRSA and *E. coli*, highlighting the crucial role of ZIF-8@PDA nanoparticles in antibacterial performance. Further, bacterial morphology observed by SEM showed that *E. coli* and MRSA exposed to NIR light alone had relatively intact bacterial membranes with no obvious damage (Fig. 3D). However, when COG-Z@P200 hydrogel was combined with NIR, the bacterial membranes exhibited wrinkling and severe damage, indicating that the photothermal effect of NIR plays a crucial role in the antibacterial activity of the hydrogel. The extent of bacterial damage increased with prolonged NIR exposure times, as evidenced by the treatments COG-Z@P200 +NIR5 and COG-Z@P200 +NIR10. And with the addition of ZIF-8@PDA and the synergistic effect of NIR, we can clearly see the nanoparticles attached to the surface of bacteria.

In *vitro* results led to the selection of MRSA for further exploration of its antibacterial mechanisms.The Zn^{2+} ion

release curve in Figure S6 was analyzed by kinetic model, revealing that the release process of Zn^{2+} was mainly controlled by diffusion (Higuchi model, $R^2 > 0.93$). The study found that the cumulative release of Zn^{2+} gradually increased over time at different pH values. Under pH 5.4 and 6.8 conditions, NIR radiation significantly accelerated the release rate of Zn^{2+}, indicating that the synergistic effect of pH environment and NIR radiation has an important influence on the Zn^{2+} release process. As reported in the literature, ZnO nanoparticles are non-toxic to the human body and have strong antibacterial activity. Photothermally enhanced ZnO nanoparticles release Zn^{2+}, promote bacterial cell membrane rupture and ROS generation to synergistically kill bacteria. This may be attributed to the protonation competition between Zn^{2+} and carboxylic acid groups under low pH conditions, resulting in the breaking of coordination bonds, thereby accelerating the release of Zn^{2+}. In addition, under the action of NIR radiation, the local temperature of the hydrogel increases, further reducing the activation energy of Zn^{2+} diffusion and accelerating the diffusion process of Zn^{2+}. NIR radiation may also promote the release of Zn^{2+} through the plasma enhancement effect. Metal nanostructures can excite local plasma resonance under NIR radiation, generate strong electric fields, enhance the reactivity of nearby molecules, further promote the release of Zn^{2+}, and significantly enhance the antibacterial properties of hydrogels. However, repeated near-infrared irradiation may affect the photothermal stability of COG-Z@P200 hydrogel. Thermal interactions may lead to the aggregation of nanoparticles due to the aggregation of nanoparticles or the oxidation effect of PDA, thereby reducing the photothermal efficiency, while the oxidation of PDA may gradually affect the structural integrity and photothermal performance of the hydrogel. The PDA coating can effectively stabilize ZIF-8 nanoparticles and mitigate the negative effects of nanoparticle aggregation and oxidation through its self-healing properties [28]. Nevertheless, these effects are mild and usually occur during longer periods of use, and do not significantly affect the short-term stability of the hydrogel. The release of Zn^{2+} is highly sensitive to pH, which helps to effectively exert antibacterial effects without compromising short-term structural stability. Similarly, the oxidation of PDA may slightly affect the mechanical strength during long-term use, but its self-healing ability can effectively offset this effect. Overall, the COG-Z@P200 hydrogel can maintain sufficient integrity during typical wound treatment processes to ensure its therapeutic effect and biocompatibility.

The TEM results, shown in Fig. 3E, revealed that the COG-Z@P200 +NIR5 treatment caused significant structural damage to the bacteria, including wrinkling of the cell membrane and leakage of cellular contents. These findings were consistent with those of other studies. The permeability of the bacterial cell membrane was further assessed using β-galactosidase, which exhibits fluorescence when the cell membrane is compromised [23]. Both the COG-Z@P200 +NIR5 and COG-Z@P200 +NIR10 treatments showed high fluorescence intensity at OD420, as demonstrated in Fig. 3F, indicating increased membrane permeability. Additionally, Fig. 3G shows a significant increase in protein leakage in MRSA treated with COG-Z@P200, while Fig. 3H shows a marked rise in ATP levels with prolonged NIR exposure. Moreover, the COG-Z@P200 +NIR5 treatment group exhibited the highest levels of leakage of cellular components, including DNA and RNA (Fig. 3I), suggesting a strong antibacterial effect. These results indicated that COG-Z@P200 combined with NIR treatment led to membrane disruption, elevated intracellular ATP levels, and ultimately, bacterial death. The effect of NIR treatment on bacterial energy consumption and intracellular ATP levels was also examined, given the strong correlation between bacterial metabolism and intracellular temperature [40, 41]. Figure 3J summarizes the proposed antibacterial mechanism of COG-Z@P hydrogel against bacteria.

Transcriptome sequence and metabolomics analysis

Transcriptome and metabolomic analysis were carried out to investigate the antibacterial mechanism of COG-Z@P200 +NIR5 on MRSA isolates in more detail. The sample group was designated as COG-Z@P200 +NIR5 for photothermal therapy, whereas the CTRL group was designated as untreated MRSA. Each sample's uniform overall gene expression levels were displayed in a boxplot (Fig. 4A), and Table S1 reported that all samples had good biological reproducibility, with all Pearson correlation coefficients better than 0.98. The findings of the transcriptome comparison show which genes are differentially expressed (DEGs) in the various groups. A total of 278 down-regulated and 192 up-regulated genes were identified within the 470 differentially expressed gene sets (FC > 2, FDR < 0.05) (Fig. 5B–C).

Gene Ontology (GO) analysis and pathway enrichment from the Kyoto Encyclopedia of Genes and Genomes (KEGG) were used to clarify the connection between differentially expressed genes (DEGs) and antibacterial action. The DEGs were functionally annotated using GO enrichment analysis, which categorized them into groups such molecular functions (MF), cellular components (CC), and biological processes (BP) (Fig. 4D). The majority of the enriched genes were linked to biological processes that included glycolysis, arginine catabolism, ATP biosynthesis, translation,

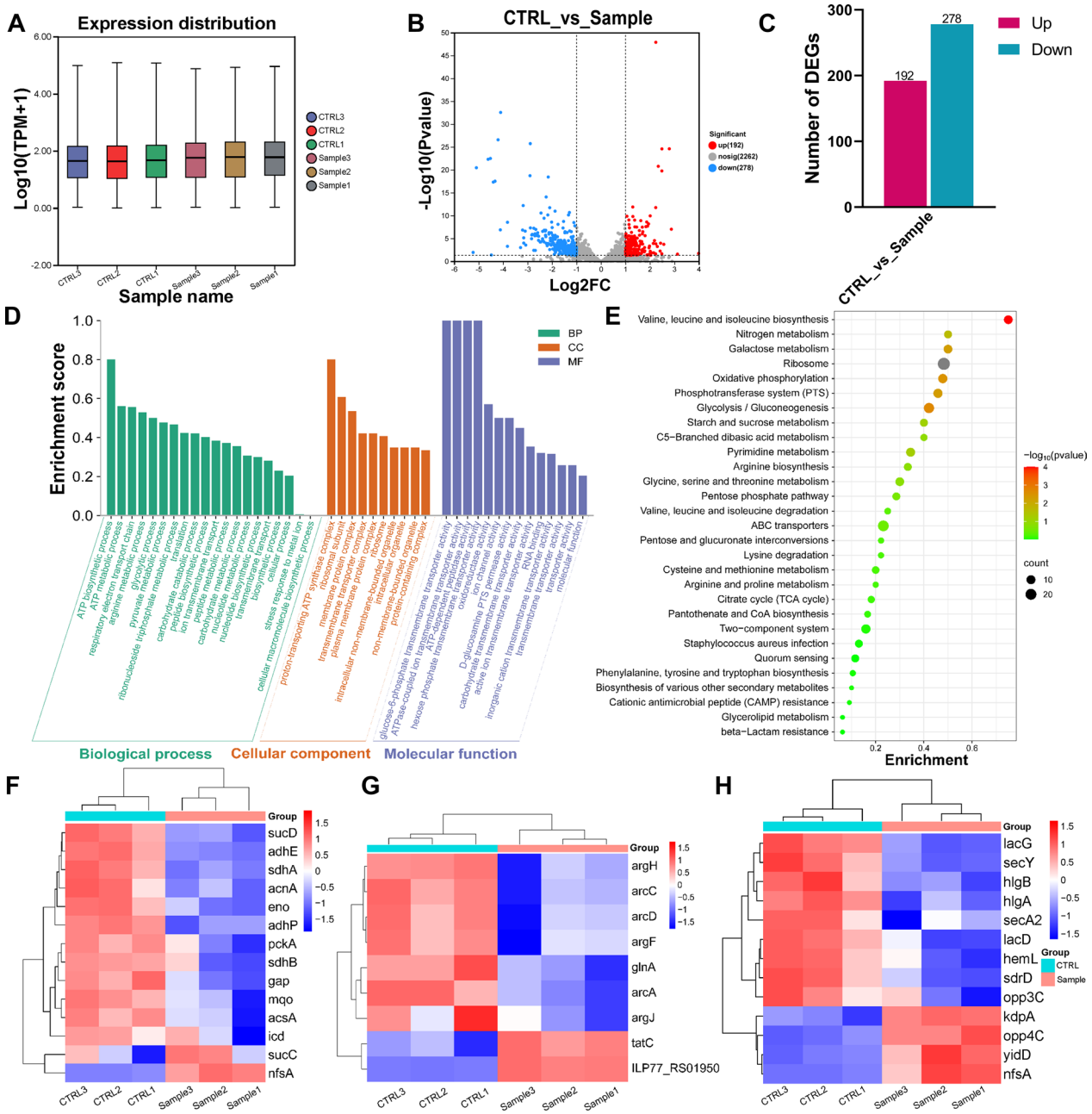

Fig. 4 Transcriptome of MRSA after different treatments with hydrogel. **A** Box plot of the expression number of DEGs; **B** Volcano plot showing the identified up- and down-regulated genes. **C** Statistical histogram of DEGs. **D** GO enrichment analysis of DEGs. **E** KEGG pathway enrichment analysis of DEGs. **F** Heatmap and cluster analysis of glycolysis and TCA-related genes. **G** Heatmap and cluster analysis of arginine-related genes. **H** Heatmap and cluster analysis of quorum sensing and virulence factor-related genes

ion transmembrane transport, macromolecule biosynthesis, and catabolic processes. Enriched genes were predominantly associated with membrane protein complexes, ribosomes, and proton-transporting ATP synthase complexes under the cellular component category. In terms of molecular function, the DEGs were mostly engaged in the transmembrane transporter activity of glucose-6-phosphate, the transmembrane transporter activity of ATPase-coupled ions, the activity of ATP-dependent peptidase, and a variety of other transmembrane transport activities, including those involving carbohydrates. Important pathways such ABC transporters, glycolysis/gluconeogenesis, the tricarboxylic acid (TCA) cycle, two-component systems,

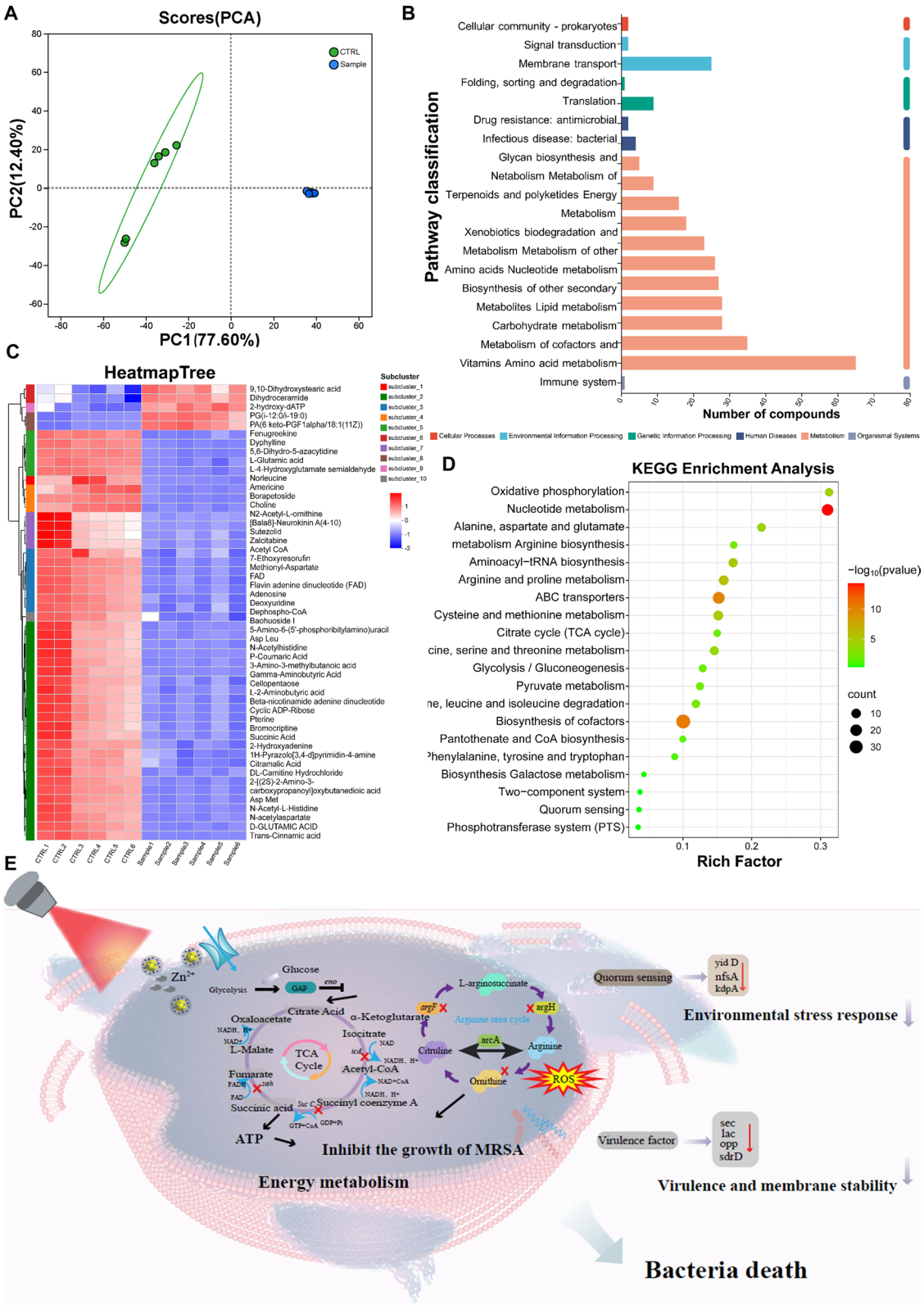

Fig. 5 Changes in MRSA metabolomics after different treatments. **A** PCA analysis of samples; **B** Column plot of enriched pathways. **C** Metabolite heat map cluster analysis. **D** KEGG pathway enrichment analysis. **E** Antimicrobial mechanism diagram of COG-Z@P200 hydrogel

and arginine biosynthesis were identified by KEGG enrichment analysis (Fig. 4E). The metabolism of galactose, the phosphotransferase system (PTS), the production of valine, leucine, and isoleucine, Staphylococcus aureus infection, quorum sensing, and the metabolism of starch and sucrose were among the other noteworthy processes. These results imply that Zn^{2+} release caused by COG-Z@P200 + NIR5 therapy, which probably interferes with protein production and jeopardizes membrane integrity in MRSA, may be responsible for the antibacterial effects seen [42]. These pathways shed light on the underlying processes of the COG-Z@P200 hydrogel's photothermal antibacterial activity.

The three main categories of antibacterial processes associated with DEGs were glycolysis, arginine biosynthesis, and quorum sensing/virulence factors. As demonstrated in Fig. 4F, the reduction in ATP generation caused by the downregulation of glycolysis-related genes (*eno, gap*) has an impact on MRSA's energy supply [43, 44]. The TCA cycle-related genes *sucC, sdhA* and *icd* were inhibited, which reduced bacterial metabolism and oxidative stress tolerance [45, 46]. Downregulation of *arcA, arcC* and *arcD* interfered with arginine biosynthesis, which is necessary for the development of biofilms and reduced MRSA's pathogenic potential (Fig. 4G) [47, 48]. The downregulation of *sec, lac, opp* and *sdrD* genes resulted in lower virulence and biofilm stability, as demonstrated in Fig. 4H, indicating that quorum sensing, which controls virulence factors, was also impacted [49]. The response of MRSA to environmental stress was shown by the upregulation of stress-related genes (*yidD, nfsA and kdpA*) [50]. According to these results, treatment with COG-Z@P200 + NIR5 suppresses MRSA development by interfering with energy metabolism, biofilm formation, and expression of virulence.

PCA analysis (Fig. 5A) showed clear differences between the CTRL and Sample groups, with strong sample correlation (Figure S7), according to metabolic analysis. Glycolysis/gluconeogenesis, pyruvate metabolism, TCA cycle, arginine and proline metabolism, ABC transport, galactose metabolism, the two-component system, PTS, and quorum sensing were identified as important metabolic pathways by KEGG pathway classification analysis (Fig. 5B, D). The heatmap clustering results revealing that COG-Z@P200 hydrogel exhibits antibacterial action against MRSA are compatible with the downregulation of metabolites such as N_2-acetyl-L-ornithine, norleucine, aspartate, methionine, and succinat (Fig. 5C). These results suggest a possible antimicrobial mechanism of COG-Z@P200 hydrogel against MRSA isolates (Fig. 5E).

Biocompatibility and antioxidant capacity

In order to systematically evaluate the cell compatibility of the hydrogel, we cultured L929 fibroblasts in the presence of different concentrations of ZIF-8 and ZIF-8@PDA nanoparticles (Fig. 6A–B). The results showed that ZIF-8@PDA NPs had no obvious toxicity to cells in the concentration range of 200 μg/mL and below, and the cell activity was maintained at a high level during the three-day culture process, which was significantly better than the unmodified ZIF-8 NPs, which had already shown certain cytotoxicity at the same concentration. This shows that dopamine modification can effectively improve the biocompatibility of ZIF-8 nanoparticles.

In addition, the MTT assay (Fig. 6C) and live/dead staining results (Fig. 6D) of the hydrogel system as a whole further verified its excellent cell compatibility. The cell viability of all groups was close to that of the 10% FBS control group, and there was almost no obvious cell death (green is live cells, red is dead cells).

Further observing the effect of different concentrations on therapeutic performance, we combined the thermal response experimental data in Fig. 2K–M and found that a ZIF-8@PDA concentration of 200 μg/mL has an ideal photothermal conversion efficiency under near-infrared laser irradiation, can quickly raise the temperature to a therapeutic window of 40–45 °C, and maintain thermal stability in multiple rounds of illumination cycles without aggregation or degradation. Therefore, this concentration not only ensures cell safety, but also meets the functional requirements of photothermal therapy. Based on the above results, 200 μg/mL was finally selected as the loading concentration of ZIF-8@PDA NPs to ensure that COG-Z@P200 hydrogel has both good therapeutic performance and biosafety, and has the potential for clinical transformation as a wound dressing.

Blood compatibility is a crucial property for biomedical hydrogels. In the hemolysis assay, PBS and 0.1% Triton X-100 were used as the negative and positive controls, respectively. Figure 6E shows that neither the COG-Z@P200 hydrogel group nor the negative control group exhibited significant hemolysis after one hour of incubation with diluted whole blood (the supernatant remained clear). In contrast, the positive control group, containing 0.1% Triton, exhibited a distinct red supernatant, indicating red blood cell rupture and hemoglobin release. The hemolysis rates of all hydrogel groups were well below the safe threshold of 5.0%, as determined by absorbance measurement at 540 nm, confirming the excellent blood compatibility of the hydrogels (Fig. 6F).

In the diabetic mouse bleeding model, bleeding was induced by puncturing the liver with a needle, and hemostasis was achieved by applying a prefabricated COG-Z@P200 hydrogel patch. Due to the hydrogel's ability to seal

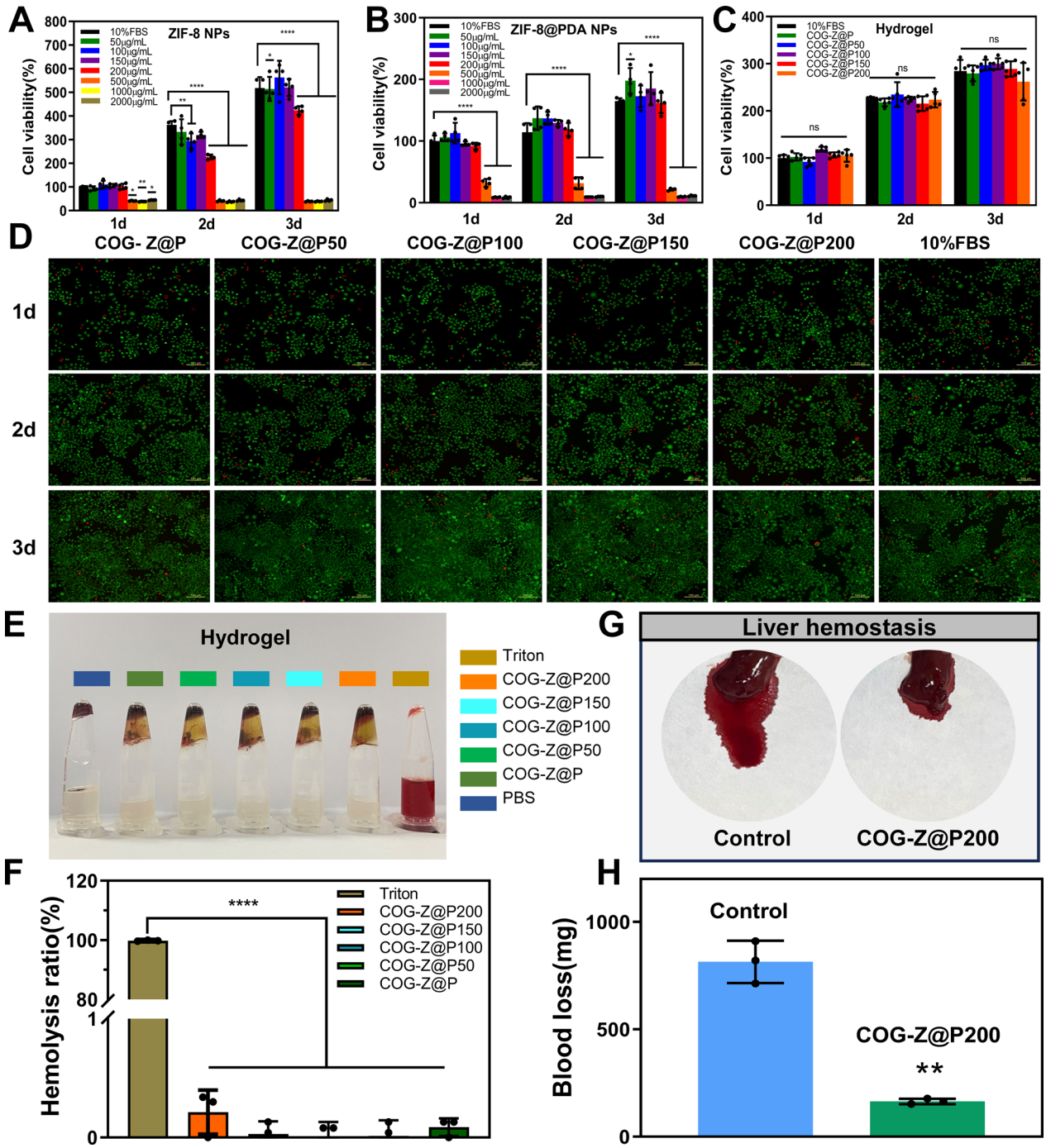

Fig. 6 Biocompatibility of ZIF-8 NPs, ZIF-8@PDA NPs and COG-Z@P composite hydrogels. **A**–**C** MTT of ZIF-8, ZIF-8@PDA and hydrogels co-cultured with L929 cells for 1, 2 and 3 days; **D** Pictures of live/dead staining of hydrogel co-cultured with L929 cells after 3 days; **E** Pictures of hemolytic activity test of hydrogel; **F** Hemolysis rate of hydrogel; **G** Pictures of hydrogel hemostatic effect; **H** Bleeding quantitative statistics. n = 3, $^{**}p < 0.01$, $^{****}P < 0.0001$

the wound and stop the bleeding, it significantly reduced liver hemorrhage (Fig. 6G). As shown in Fig. 6H, blood loss in the COG-Z@P200 hydrogel group was 111.02 mg, while the untreated control group lost 246.47 mg of blood, indicating the hydrogel's effective hemostatic properties.

The ROS-scavenging capability of the hydrogel was assessed by co-culturing it with L929 fibroblasts treated

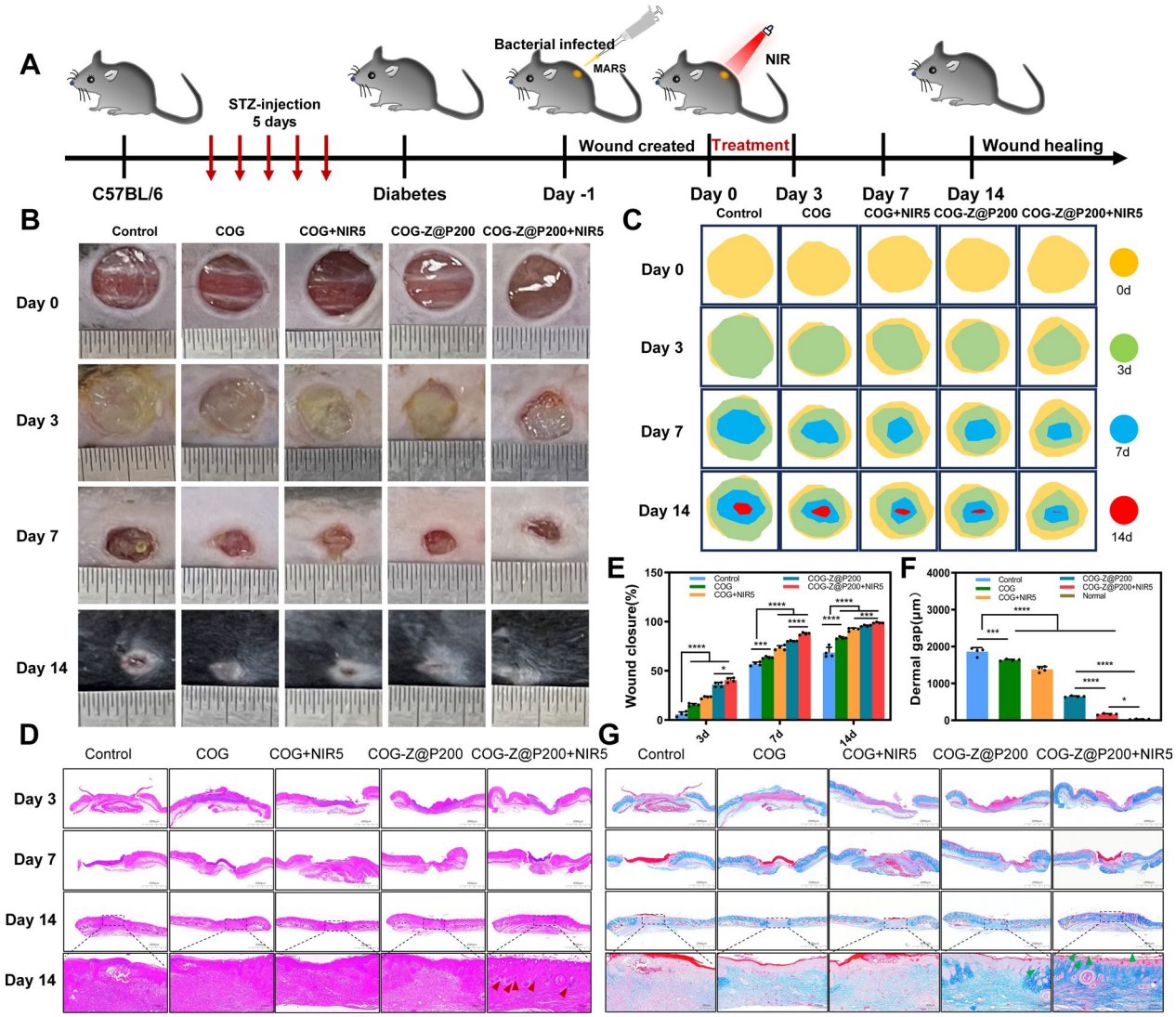

Fig. 7 COG-Z@P200 hydrogel promotes wound healing. **A** Establishment of MASA-infected diabetic wound model; **B** Pictures of wound healing; **C** Wound healing simulation diagram; **D** H&E staining images; **E** Wound healing rate; **F** Dermal gap; **G** Masson staining images. **P < 0.05, ***P < 0.001, ****P < 0.0001*

with the ROS inducer Rosup. In addition to stimulating excessive ROS production, Rosup enables the quantification of intracellular ROS levels using the DCFH-DA fluorescent probe. As shown in Figure S8, the positive control group (treated with Rosup alone) exhibited a significant increase in fluorescence intensity, indicating elevated ROS levels. In contrast, treatment with 5 mg/mL COG-Z@P200 hydrogel markedly reduced fluorescence intensity, suggesting effective ROS scavenging. These findings demonstrate that COG-Z@P200 hydrogel can efficiently mitigate oxidative stress, highlighting its potential as a wound dressing for managing ROS-related tissue damage.

Full thickness MRSA infected skin wound healing

To establish a subcutaneous infection model, full-thickness skin defects were created on the dorsal regions of mice, and wound healing was monitored following hydrogel treatment at days 0, 3, 7 and 14 (Fig. 7A). No adverse effects were observed in any animal group throughout the procedure. Representative wound images at different time points (0, 3, 7 and 14 days) are shown in Fig. 7B–C, with the COG-Z@P200 + NIR5 group exhibiting the smallest wound area.

Histological analysis via H&E staining (Fig. 7D) revealed inflammatory cell infiltration in all groups by day 3, marking the inflammatory phase. By day 7,

new epidermis formation was evident in the COG-Z@P200 and COG-Z@P200 + NIR5 groups, with the latter exhibiting more pronounced healing. In the COG, COG + NIR5, and COG-Z@P200 groups, scab formation was observed, accompanied by epithelial and inflammatory cell migration toward the wound center. However, in the control group, neither epidermal regeneration nor significant healing was observed.

By day 14, the COG-Z@P200 group had entered the remodeling phase, exhibiting a thicker epidermal layer and a narrower dermal gap compared to the control and NIR groups. In the COG-Z@P200 + NIR5 group, tissue remodeling was nearly complete, with the dermal structure closely resembling that of normal skin and the formation of numerous hair follicles, indicating advanced healing. High-magnification images of tissue sections (Fig. 7D) revealed the emergence of new hair follicles in the dermis of the COG-Z@P200 group, whereas the control and COG groups displayed a thicker epithelial layer with delayed dermal remodeling. Notably, in the COG-Z@P200 + NIR5 group, the dermis underwent more rapid maturation, characterized by the presence of abundant newly formed hair follicles (red arrows) and a thinner, more structurally normal epithelial layer. These findings demonstrate that both the COG-Z@P200 and COG-Z@P200 + NIR5 groups significantly outperformed the control and NIR groups in promoting wound healing. The superior wound healing observed in the COG-Z@P200 + NIR group is likely attributed to its photothermal antibacterial effects, which facilitated epithelialization and accelerated dermal tissue maturation.

The wound healing rate (Fig. 7E) indicated that the COG-Z@P200 + NIR5 group exhibited significantly accelerated wound closure compared to other groups at days 3, 7 and 14. By day 14, the epidermal thickness in the control, COG, COG + NIR5, and COG-Z@P200 groups remained markedly different from that of normal skin tissue, whereas the epidermal thickness in the COG-Z@P200 + NIR5 group closely resembled that of normal skin (Figure S9). Moreover, the COG-Z@P200 + NIR5 group displayed the smallest dermal gap (135.2 μm) among all groups, approximating the normal skin tissue gap (Fig. 7F), suggesting that COG-Z@P200 + NIR5 significantly promoted dermal tissue repair. The Masson staining results of the wound sites in each group are shown in Fig. 7G. On day 3, only a small amount of collagen deposition was observed in localized regions of the wound areas in all groups. Notably, the collagen content in the COG-Z@P200 + NIR5 group was significantly higher than in the other groups, indicating that this group exhibited stronger collagen synthesis ability during the early stages of wound healing. By day 7, the number of fibroblasts had generally increased in all groups, but significant differences were observed in the distribution pattern of collagen fibers. In the Control and COG groups, collagen fibers were mainly concentrated on the sides of the wound, while the collagen deposition in the area beneath the wound was sparse. In contrast, the COG-Z@P200 and COG-Z@P200 + NIR5 groups exhibited more prominent collagen deposition in the granulation tissue, with a more uniform distribution. Among these, the COG-Z@P200 + NIR5 group showed the most intense collagen staining, suggesting its superior collagen synthesis capacity.

Histological analysis of internal organs using H&E staining (Figure S10) revealed severe organ damage in the control group, including cardiac rupture (blue arrow), hepatic sinusoidal dilation (black arrow), indistinct red and white pulp junctions in the spleen (white circles), inflammatory infiltration in the lungs (yellow circles), renal tubular dilation (blue arrows), and vacuolar degeneration. In contrast, mice treated with COG-Z@P200 + NIR5 exhibited no signs of inflammatory infiltration, and their internal organs appeared histologically normal. These findings indicate that the COG-Z@P200 + NIR5 hydrogel possesses excellent biocompatibility and does not induce systemic toxicity, underscoring its potential for safe in vivo applications.

Antibacterial and microenvironmental regulation in vivo

In vivo investigation was conducted to assess the antibacterial efficacy and tissue integration of COG-Z@P200 under near-infrared (NIR) radiation. On the third day, wound tissue was excised to examine bacterial growth at the wound site through Gram staining. The results, presented in Fig. 8A, indicated a noticeable purple coloration in the control and COG groups, suggesting significant bacterial presence and potential ongoing infection. In contrast, the COG + NIR5 and COG-Z@P200 groups exhibited much less purple staining, indicating a reduction in bacterial infection. The COG-Z@P200 + NIR5 group showed almost no purple staining, reflecting the substantial bacterial clearance, which aligns with previous in vitro antibacterial results. Further, bacterial cultures from the skin surface (Fig. 8B–C) revealed that the COG-Z@P200 + NIR5 group had almost no bacterial colonies, corresponding to an antibacterial rate of up to 98%. Analysis of live and dead bacteria in the collected bacterial solution (Fig. 8D) demonstrated a significantly higher proportion of dead bacteria in the COG-Z@P200 + NIR5 group. These results confirm that the incorporation of ZIF-8@PDA nanoparticles and NIR irradiation enhanced the antibacterial properties of the hydrogel.

In order to systematically evaluate the comprehensive regulatory effects and in vivo safety of COG-Z@P200 hydrogel in diabetic wound repair, we focused on analyzing its effects on immunomodulation, angiogenesis, and

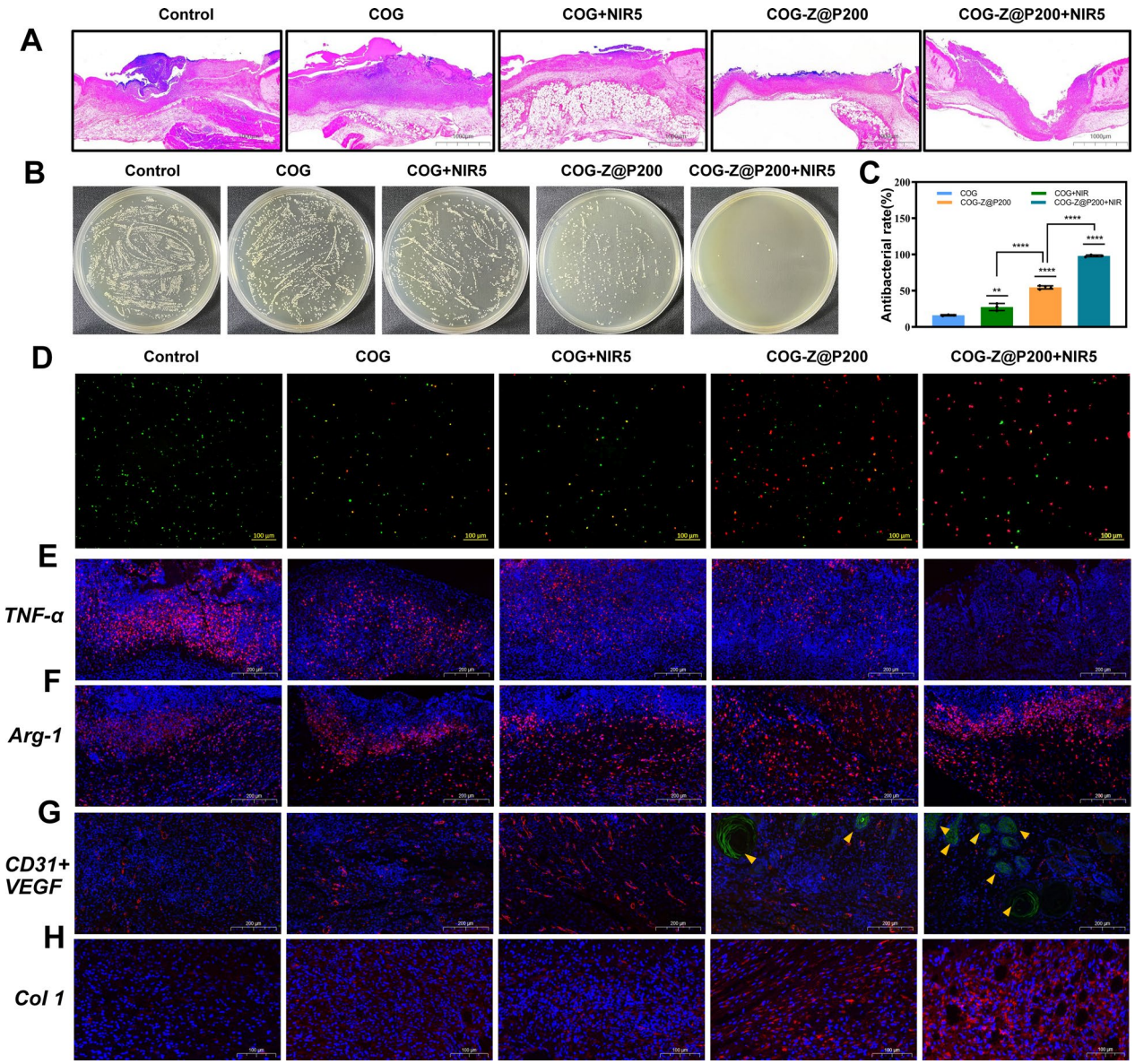

Fig. 8 Microenvironmental status of the wound site. **A** Gram staining of bacteria (G+ : purple; G−: red); **B** Photos of bacterial colonies; **C** Antibacterial rate; **D** Staining of live and dead bacteria. **E**–**F** Immunofluorescence staining of TNF-α (red) and Arg-1 (red) at the wound site on 7 th day; **G**–**H** Immunofluorescence staining of CD31 (red), VEGF (green) and Col1 (red) on 14 th day. (Blue fluorescence indicates cell nuclei) ***$P < 0.001$, ****$P < 0.0001$

collagen deposition. As shown in Fig. 8E, F, the immunofluorescence staining results showed that COG-Z@P200 hydrogel could effectively inhibit the expression of proinflammatory factor TNF-α, while upregulating Arg-1, promoting the polarization of macrophages from M1 to M2, alleviating inflammatory response, and accelerating the transformation of wounds from the inflammatory phase to the repair phase. The expression of angiogenesis markers CD31 and VEGF was enhanced, and green ring structures appeared, indicating that the new blood vessels gradually matured and the vascularization level was significantly improved (Fig. 8G). In addition, as shown in Fig. 8H, the immunofluorescence staining results of type I collagen showed that COG-Z@P200 and its combined NIR irradiation group significantly enhanced collagen deposition on the 14 th day, which is related to tissue repair, further verifying the role of hydrogel in promoting connective tissue regeneration. Overall, COG-Z@P200 hydrogel synergistically regulates the wound microenvironment through multiple mechanisms, significantly promoting the healing of diabetic infected wounds.

To investigate the biodegradability of the hydrogels, we conducted a systematic exploration of their degradation kinetics by simulating various wound microenvironment conditions (including pH, enzyme presence, and ROS levels) through in vitro experiments. The experimental results showed that the degradation rate of hydrogels was closely related to the intensity of microenvironmental stimulation. In the pH-dependent degradation experiment (Figure S11 A), the acidic environment significantly accelerated the degradation. Under pH 5.4 conditions, the residual mass of the hydrogel dropped to 30% within 7 days, while the degradation rate was significantly slowed down under neutral (pH 6.8) and weakly alkaline (pH 7.4) environments. In the enzymatic degradation experiment (Figure S11B), the higher the lysosome concentration, the stronger the degradation effect. The 1.0 mg/mL lysosome treatment group had only 20% of the residual mass on the 7th day, which was more thoroughly degraded than the 0.5 mg/mL group. In the oxidative stress experiment (Figure S11 C), when the hydrogen peroxide concentration increased from 1.0 to 10.0 mM, the residual mass decrease rate of the hydrogel increased by nearly 3 times, and the high concentration ROS environment significantly destroyed the stability of the material. Similarly, the hydrogels were implanted subcutaneously to observe their decomposition over time. By day 14, the hydrogels had completely degraded (Figure S12 A). Histological examination using H&E and Masson staining (Figure S12B–C) showed that the COG-Z@P200-treated tissues did not show obvious inflammatory responses compared with the control group. Obvious collagen deposition was seen in the treated tissues, and after 14 days, there was no significant difference between the treated tissues and the surrounding normal tissues. To evaluate the antioxidant properties of the hydrogels in vivo, dihydroethidium (DHE) staining was performed on the third day to assess the intracellular ROS levels at the wound site (Figure S13). Compared with the control group, the red fluorescence of ROS staining was significantly reduced in the COG-Z@P200 and COG-Z@P200 + NIR5 hydrogel groups, indicating that the COG-based hydrogels have excellent antioxidant capacity.

Discussion

A multicomponent synergistic photothermal hydrogel dressing (COG-Z@P200) was engineered for the treatment of methicillin-resistant MRSA infected wounds, combining robust antibacterial activity with exceptional tissue compatibility. The hydrogel achieves its bactericidal efficacy through a dual-action mechanism involving Zn^{2+}-mediated membrane destabilization and near-infrared (NIR)-activated mild photothermal therapy (PTT). Specifically, Zn^{2+} ions released from COG-Z@P200 hydrogel electrostatically interact with the negatively charged bacterial membrane, inducing structural permeabilization. Concurrently, under NIR irradiation, localized hyperthermia (40–45 °C) synergistically enhances membrane disruption, facilitating rapid leakage of intracellular proteins, nucleic acids (DNA/RNA), and cytoplasmic components, ultimately leading to bacterial death. Crucially, this low-temperature PTT strategy can maintain the integrity of healthy tissue while maximizing antibacterial efficiency, effectively avoiding the thermal damage that may occur in traditional photothermal therapy [51, 52]. NIR light is an ideal trigger due to its good penetration and non-invasiveness [53].

Mechanistically, transcriptomic and metabolomic profiling revealed that COG-Z@P200 hydrogel disrupts MRSA pathogenicity via multimodal metabolic interference. Specifically, it suppresses glycolysis, blocks the tricarboxylic acid (TCA) cycle, and impairs arginine biosynthesis, thereby inducing DNA fragmentation and metabolic collapse. Concurrently, the hydrogel inhibits biofilm formation by downregulating quorum sensing-related genes (e.g., *agr*, *operon*) and suppresses cell membrane synthesis through fatty acid metabolism inhibition.

In vivo evaluations in diabetic murine models demonstrated the COG-Z@P200 hydrogel's therapeutic superiority through coordinated antioxidant, anti-inflammatory, and pro-regenerative mechanisms. DHE staining confirmed the hydrogel's potent ROS scavenging capacity, significantly attenuating oxidative stress in wound tissues. Concurrent immunofluorescence analysis revealed upregulated Arg-1 expression and suppressed TNF-α levels, indicating M2 macrophage polarization and resolution of chronic inflammation. These effects synergistically preserved fibroblast functionality, enhanced angiogenesis (evidenced by elevated VEGF/CD31 expression), and promoted structured collagen deposition (as demonstrated via Masson's trichrome staining), collectively accelerating wound closure compared to conventional treatments. By concurrently remodeling oxidative, inflammatory, and metabolic microenvironments, the COG-Z@P200 hydrogel establishes a multifunctional paradigm for combating drug-resistant infections in diabetic wounds.

Compared with other wound dressings based on similar hydrogels (such as chitosan-based, collagen-based, or silver nanoparticle-loaded hydrogels), COG-Z@P200 + NIR5 hydrogel exhibits clear advantages in terms of its dual antibacterial mechanisms (Zn^{2+} release and photothermal effect), strong mechanical properties, biodegradability, and exceptional wound healing potential (Table S2). Additionally, compared to the commonly used clinical antibiotic vancomycin, COG-Z@

P200 + NIR5 hydrogel demonstrates broader-spectrum antibacterial activity, faster wound healing, and a dual-mode mechanism that prevents bacterial resistance. Notably, vancomycin is associated with various adverse effects, including nephrotoxicity, infusion-related "red man syndrome," and ototoxicity from prolonged or high-dose use. In contrast, COG-Z@P200 + NIR5 hydrogel shows excellent biocompatibility, very low cytotoxicity, and does not require systemic administration, thus avoiding the risk of systemic side effects. These advantages highlight the potential of this hydrogel as a safe and effective non-antibiotic alternative for treating infected diabetic wounds. In summary, COG-Z@P200 hydrogel has good scalability, mature production process, and is suitable for large-scale production. Sterilization can be done by pasteurization, and freeze-dried storage at −80 °C is recommended to maintain its stability. Regarding regulation, it is expected to be approved as a Class II medical device in the United States and may be approved as a Class III medical device in the European Union, which requires clinical trial verification.

Supplementary Information

The online version contains supplementary material available at https://doi.org/10.1186/s12951-025-03451-6.

Additional file 1.

Acknowledgements
We thank the Natural Science Basic Research Program of Shaanxi (2024 JC-YBMS-657, 2023-JC-YB-290) and Innovation Foundation for Doctor Dissertation of Northwestern Polytechnical University (CX2024081) for financial support. We express our gratitude to the Experimental Center of the School of Life Sciences at Northwestern Polytechnical University for their assistance in our research on cellular testing.

Author contributions
QG, conceived and designed experiments. FFH, helped design Fig. 1, assisted experiment. ZHC, CYZ, WHZ, KP, ZYY, participated in the experimental process, analysed results. YNZ, RS, XLW, helped guide the experiment. QG and TLL wrote the manuscript. All the authors reviewed the manuscript.

Funding
We thank the Natural Science Basic Research Program of Shaanxi (2024 JC-YBMS-657, 2023-JC-YB-290) and Innovation Foundation for Doctor Dissertation of Northwestern Polytechnical University (CX2024081) for financial support. We express our gratitude to the Experimental Center of the School of Life Sciences at Northwestern Polytechnical University for their assistance in our research on cellular testing.

Availability of data and materials
No datasets were generated or analysed during the current study.

Declarations

Ethics approval and consent to participate
All husbandry and animal methodologies conformed to the ethical standards stipulated in the National Research Council's Guide for the Care and Use of Laboratory Animals and were approved by the Animal Ethics Committee of Northwestern Polytechnical University (Approval No. 202202091), ensuring humane practices in animal handling.

Consent for publication
All authors agree to be published.

Competing interests
The authors declare no competing interests.

Author details
[1]Key Laboratory of Space Bioscience and Biotechnology, Engineering Research Center of Chinese Ministry of Education for Biological Diagnosis, Treatment and Protection Technology and Equipment, School of Life Sciences, Northwestern Polytechnical University, No. 1 Dongxiang Road, Chang'an District, Xi'an City 710129, People's Republic of China. [2]Department of Mechanical Engineering, College of Design and Engineering, National University of Singapore, 21 Lower Kent Ridge Road, Singapore 117574, Singapore.

Received: 22 February 2025 Accepted: 5 May 2025
Published online: 26 May 2025

References

1. Xu Q, Chang M, Zhang Y, Wang E, Xing M, Gao L, Huan Z, Guo F, Chang J. PDA/Cu bioactive hydrogel with "Hot Ions Effect" for inhibition of drug-resistant bacteria and enhancement of infectious skin wound healing. ACS Appl Mater Interfaces. 2020;12:31255–69.
2. Veiseh O, Tang BC, Whitehead KA, Anderson DG, Langer R. Managing diabetes with nanomedicine: challenges and opportunities. Nat Rev Drug Discov. 2015;14:45–57.
3. Dong X, Ye J, Chen Y, Tanziela T, Jiang H, Wang X. Intelligent peptide-nanorods against drug-resistant bacterial infection and promote wound healing by mild-temperature photothermal therapy. Chem Eng J. 2022;432:134061.
4. Wang ZF, Peng YL, Zhou Y, Zhang SN, Tan JX, Li H, He DG, Deng L. Pd-Cu nanoalloy for dual stimuli-responsive chemo-photothermal therapy against pathogenic biofilm bacteria. Acta Biomater. 2022;137:276–89.
5. Singh AP, Biswas A, Shukla A, Maiti P. Targeted therapy in chronic diseases using nanomaterial-based drug delivery vehicles. Signal Transduct Target Ther. 2019;4:33.
6. Holl J, Kowalewski C, Zimek Z, Fiedor P, Kaminski A, Oldak T, Moniuszko M, Eljaszewicz A. Chronic diabetic wounds and their treatment with skin substitutes. Cells. 2021;10:655.
7. Yang X, Li J, Chen X, Wang T, Li G, Zhang K, Yin J, Cui H. Multifunctional hydrogels for wound healing. 2024;44:173–94.
8. Chen R, Wang P, Xie J, Tang Z, Fu J, Ning Y, Zhong Q, Wang D, Lei M, Mai H, et al. A multifunctional injectable, self-healing, and adhesive hydrogel-based wound dressing stimulated diabetic wound healing with combined reactive oxygen species scavenging, hyperglycemia reducing, and bacteria-killing abilities. J Nanobiotechnol. 2024;22:444.
9. Zare H, Rezayi M, Aryan E, Meshkat Z, Hatmaluyi B, Neshani A, Ghazvini K, Derakhshan M, Sankian M. Nanotechnology-driven advances in the treatment of diabetic wounds. Biotechnol Appl Biochem. 2021;68:1281–306.
10. Rayate AS, Nagoba BS, Mumbre SS, Mavani HB, Gavkare AM, Deshpande AS. Current scenario of traditional medicines in management of diabetic foot ulcers: a review. World J Diabetes. 2023;14:1–16.
11. Xia H, Dong Z, Tang Q, Ding R, Bai Y, Zhou K, Wu L, Hao L, He Y, Yang J, et al. Glycopeptide-based multifunctional hydrogels promote diabetic wound healing through pH regulation of microenvironment. Adv Funct Mater. 2023;33.
12. Halawa EM, Fadel M, Al-Rabia MW, Behairy A, Nouh NA, Abdo M, Olga R, Fericean L, Atwa AM, El-Nablaway M, Abdeen A. Antibiotic action and resistance: updated review of mechanisms, spread, influencing factors, and alternative approaches for combating resistance. Front Pharmacol. 2024;14.
13. Xie G, Wang X, Mo M, Zhang LB, Zhu JT. Photothermal hydrogels for promoting infected wound healing. Macromol Biosci. 2023;23.
14. Yang Y, Zhong S, Meng F, Cui X. Multi-functional hydrogels to promote diabetic wound healing: a review. Chem Eng J. 2024;497.

15. Chen Y, Gao Y, Chen Y, Liu L, Mo A, Peng Q. Nanomaterials-based photothermal therapy and its potentials in antibacterial treatment. J Control Release. 2020;328:251–62.
16. Xu J-W, Yao K, Xu Z-K. Nanomaterials with a photothermal effect for antibacterial activities: an overview. Nanoscale. 2019;11:8680–91.
17. Xu Z, Wang T, Liu J. Recent development of polydopamine anti-bacterial nanomaterials. Int J Mol Sci. 2022;23:7278.
18. Zhao Y, Wang Y, Wang X, Qi R, Yuan H. Recent progress of photothermal therapy based on conjugated nanomaterials in combating microbial infections. Nanomaterials. 2023;13:2269.
19. Zha K, Zhang W, Hu W, Tan M, Zhang S, Yu Y, Gou S, Bu P, Zhou B, Zou Y, et al. Three-step regenerative strategy: multifunctional bilayer hydrogel for combined photothermal/photodynamic therapy to promote drug-resistant bacteria-infected wound healing. Adv Funct Mater. 2024;34:2308145.
20. Zeng W-N, Wang D, Yu Q-P, Yu Z-P, Wang H-Y, Wu C-Y, Du S-W, Chen X-Y, Li J-F, Zhou Z-K, Zeng Y, Zhang Y. Near-infrared light-controllable multifunction mesoporous polydopamine nanocomposites for promoting infected wound healing. ACS Appl Mater Interfaces. 2022;14:2534–50.
21. Zhao P, Zhang Y, Chen X, Xu C, Guo J, Deng M, Qu X, Huang P, Feng Z, Zhang J. Versatile hydrogel dressing with skin adaptiveness and mild photothermal antibacterial activity for methicillin-resistant staphylococcus aureus-infected dynamic wound healing. Adv Sci. 2023;10:2206585.
22. Wu Y, Liao Q, Wu L, Luo Y, Zhang W, Guan M, Pan H, Tong L, Chu PK, Wang H. ZnL2-BPs integrated bone scaffold under sequential photothermal mediation: a Win-Win strategy delivering antibacterial therapy and fostering osteogenesis thereafter. ACS Nano. 2021;15:17854–69.
23. Kermanian M, Nadri S, Mohammadi P, Iravani S, Ahmadi N, Alinezhad V, Shokrgozar M-A, Haddad M, Mostafavi E, Maleki A. Zeolitic imidazolate frameworks: from bactericidal properties to tissue regeneration. J Control Release. 2023;359:326–46.
24. Liu B, Yang Y, Wu H, Wang S, Tian J, Dai C, Liu T. Zeolitic imidazolate framework-8 triggers the inhibition of arginine biosynthesis to combat methicillin-resistant *Staphylococcus aureus*. Small. 2023;19:2205682.
25. Ren X, Chang L, Hu Y, Zhao X, Xu S, Liang Z, Mei X, Chen Z. Au@MOFs used as peroxidase-like catalytic nanozyme for bacterial infected wound healing through bacterial membranes disruption and protein leakage promotion. Mater Des. 2023;229:111890.
26. Jiang Z, Li J, Wang J, Pan Y, Liang S, Hu Y, Wang L. Multifunctional fucoidan-loaded Zn-MOF-encapsulated microneedles for MRSA-infected wound healing. J Nanobiotechnol. 2024.
27. Huo J, Jia Q, Huang H, Zhang J, Li P, Dong X, Huang W. Emerging photothermal-derived multimodal synergistic therapy in combating bacterial infections. Chem Soc Rev. 2021;50:8762–89.
28. Qi X, Huang Y, You S, Xiang Y, Cai E, Mao R, Pan W, Tong X, Dong W, Ye F, Shen J. Engineering robust Ag-decorated polydopamine nano-photothermal platforms to combat bacterial infection and prompt wound healing. Adv Sci. 2022;9:2106015.
29. Liu Z, Guo K, Yan L, Zhang K, Wang Y, Ding X, Zhao N, Xu F-J. Janus nanoparticles targeting extracellular polymeric substance achieve flexible elimination of drug-resistant biofilms. Nat Commun. 2023;14:5132.
30. Kong L, Lv S, Qiao Z, Yan Y, Zhang J, Bi S. Metal-organic framework nanoreactor-based electrochemical biosensor coupled with three-dimensional DNA walker for label-free detection of microRNA. Biosens Bioelectron. 2022;207:114188.
31. Venna SR, Carreon MA. Highly permeable zeolite imidazolate framework-8 membranes for CO_2/CH_4 separation. J Am Chem Soc. 2010;132:76.
32. Zhou L, Li N, Owens G, Chen Z. Simultaneous removal of mixed contaminants, copper and norfloxacin, from aqueous solution by ZIF-8. Chem Eng J. 2019;362:628–37.
33. Luo D, Li C, Zhang Y, Ma Q, Ma C, Nie Y, Li M, Weng X, Huang R, Zhao Y, et al. Design of quasi-MOF nanospheres as a dynamic electrocatalyst toward accelerated sulfur reduction reaction for high-performance lithium-sulfur batteries. Adv Mater. 2022;34:2105541.
34. Li Y, Yang Z, Sun Q, Xu R, Li R, Wu D, Huang R, Wang F, Li Y. Biocompatible cryogel with good breathability, exudate management, antibacterial and immunomodulatory properties for infected diabetic wound healing. Adv Sci. 2023;10:2304243.
35. Li C, Cheng Y, Li D, An Q, Zhang W, Zhang Y, Fu Y. Antitumor applications of photothermal agents and photothermal synergistic therapies. Int J Mol Sci. 2022;23:7909.
36. Lima-Sousa R, Alves CG, Melo BL, Costa FJP, Nave M, Moreira AF, Mendonça AG, Correia IJ, de Melo-Diogo D. Injectable hydrogels for the delivery of nanomaterials for cancer combinatorial photothermal therapy. Biomater Sci. 2023;11:6082–108.
37. Zhao H, Zhang Z, Zuo D, Li L, Li F, Yang D. A synergistic DNA-polydopamine-MnO_2 nanocomplex for near-infrared-light-powered DNAzyme-mediated gene therapy. Nano Lett. 2021;21:5377–85.
38. Li H, Wen H, Zhang Z, Song N, Kwok RTK, Lam JWY, Wang L, Wang D, Tang BZ. Reverse thinking of the aggregation-induced emission principle: amplifying molecular motions to boost photothermal efficiency of nanofibers. Angew Chem Int Ed. 2020;59:20371–5.
39. Han K, Bai Q, Zeng Q, Sun N, Zheng C, Wu W, Zhang Y, Lu T. A multifunctional mussel-inspired hydrogel with antioxidant, electrical conductivity and photothermal activity loaded with mupirocin for burn healing. Mater Des. 2022;217:110598.
40. Shen L, Xie TR, Yang RZ, Chen Y, Kang JS. Application of a dye-based mitochondrion-thermometry to determine the receptor downstream of prostaglandin E(2) involved in the regulation of hepatocyte metabolism. Sci Rep. 2018;8:13065.
41. Wang X, Yao M, Ma L, Yu P, Lu T, Zhang L, Yuan X, Zhang Y, Ye J. NIR-responsive Ti_3C_2 MXene colloidal solution for curing purulent subcutaneous infection through the "Nanothermal Blade" effect. Adv Healthcare Mater. 2021;10:2100392.
42. Xue Y, Zhang L, Liu FW, Dai F, Kong L, Ma DY, Han Y. Alkaline "Nanoswords" coordinate ferroptosis-like bacterial death for antibiosis and osseointegration. ACS Nano. 2023;17:2711–24.
43. Wang Y, Malkmes MJ, Jiang C, Wang P, Zhu L, Zhang H, Zhang Y, Huang H, Jiang L. Antibacterial mechanism and transcriptome analysis of ultrasmall gold nanoclusters as an alternative of harmful antibiotics against gram-negative bacteria. J Hazard Mater. 2021;416:126236.
44. Lee JW, Lee SY. Proteome-based physiological analysis of the metabolically engineered succinic acid producer *Mannheimia succiniciproducens* LPK7. Bioprocess Biosyst Eng. 2010;33:97–107.
45. De Backer S, Sabirova J, De Pauw I, De Greve H, Hernalsteens J-P, Goossens H, Malhotra-Kumar S. Enzymes catalyzing the TCA- and urea cycle influence the matrix composition of biofilms formed by methicillin-resistant *Staphylococcus aureus* USA300. Microorganisms. 2018;6:113.
46. Zhang S, Qu X, Jiao J, Tang H, Wang M, Wang Y, Yang H, Yuan W, Yue B. Felodipine enhances aminoglycosides efficacy against implant infections caused by methicillin-resistant *Staphylococcus aureus*, persisters and biofilms. Bioactive Mater. 2022;14:272–89.
47. Mizrahi V, Warner DF. Death of *Mycobacterium tuberculosis* by L-arginine starvation. Proc Natl Acad Sci USA. 2018;115:9658–60.
48. Zúñiga M, Champomier-Verges M, Zagorec M, Pérez-Martínez G. Structural and functional analysis of the gene cluster encoding the enzymes of the arginine deiminase pathway of *Lactobacillus sake*. J Bacteriol. 1998;180:4154–9.
49. Hiles ID, Gallagher MP, Jamieson DJ, Higgins CF. Molecular characterization of the oligopeptide permease of *Salmonella typhimurium*. J Mol Biol. 1987;195:125–42.
50. Salam LB, Obayori OS, Ilori MO, Amund OO. Chromium contamination accentuates changes in the microbiome and heavy metal resistome of a tropical agricultural soil. World J Microbiol Biotechnol. 2023;39:228.
51. Jeong CJ, Sharker SM, In I, Park SY. Iron Oxide@PEDOT-based recyclable photothermal nanoparticles with poly(vinylpyrrolidone) sulfobetaines for rapid and effective antibacterial activity. ACS Appl Mater Interfaces. 2015;7:9469–78.
52. Kim SH, Kang EB, Jeong CJ, Sharker SM, In I, Park SY. Light controllable surface coating for effective photothermal killing of bacteria. ACS Appl Mater Interfaces. 2015;7:15600–6.
53. Rahman M, Chowdhury F, Uddin K, Ahmed KS, Hossain H, Jain P, Reza HM, Lee K, Sharker SM. Nanostructured chitosan-polyphenolic patch for remote NIR-photothermal controlled dermal drug delivery. Int J Biol Macromol. 2023;241:124701.

Publisher's Note